

Masses, Radii, and Cloud Properties of the HR 8799 Planets

Mark S. Marley

NASA Ames Research Center, MS-245-3, Moffett Field, CA 94035, U.S.A.;
Mark.S.Marley@NASA.gov

Didier Saumon

Los Alamos National Laboratory, Mail Stop F663, Los Alamos NM 87545;
dsaumon@lanl.gov

Michael Cushing

Department of Physics and Astronomy, The University of Toledo, 2801 West Bancroft
Street, Toledo, OH 43606; michael.cushing@gmail.com

Andrew S. Ackerman

andrew.ackerman@nasa.gov

Jonathan J. Fortney

Department of Astronomy and Astrophysics, University of California, Santa Cruz, CA
95064; jfortney@ucolick.org

and

Richard Freedman

SETI Institute & NASA Ames Research Center, MS-245-3, Moffett Field, CA 94035,
U.S.A.; freedman@darkstar.arc.nasa.gov

ABSTRACT

The near-infrared colors of the planets directly imaged around the A star HR 8799 are much redder than most field brown dwarfs of the same effective temperature. Previous theoretical studies of these objects have compared the photometric and limited spectral data of the planets to the predictions of various atmosphere and evolution models and concluded that the atmospheres of planets b, c, and d are unusually cloudy or have unusual cloud properties. Most studies have also found that the inferred radii of some or all of the planets disagree with

expectations of standard giant planet evolution models. Here we compare the available data to the predictions of our own set of atmospheric and evolution models that have been extensively tested against field L and T dwarfs, including the reddest L dwarfs. Unlike almost all previous studies we specify mutually self-consistent choices for effective temperature, gravity, cloud properties, and planetary radius. This procedure yields plausible and self-consistent values for the masses, effective temperatures, and cloud properties of all three planets. We find that the cloud properties of the HR 8799 planets are in fact not unusual but rather follow previously recognized trends including a gravity dependence on the temperature of the L to T spectral transition, some reasons for which we discuss. We find that the inferred mass of planet b is highly sensitive to the H and K band spectrum. Solutions for planets c and particularly d are less certain but are consistent with the generally accepted constraints on the age of the primary star and orbital dynamics. We also confirm that as for L and T dwarfs and solar system giant planets, non-equilibrium chemistry driven by atmospheric mixing is also important for these objects. Given the preponderance of data suggesting that the L to T spectral type transition is gravity dependent, we present a new evolution calculation that predicts cooling tracks on the near-infrared color-magnitude diagram. Finally we argue that the range of uncertainty conventionally quoted for the bolometric luminosity of all three planets is too small.

Subject headings: brown dwarfs — planetary systems — stars: atmospheres — stars: low mass, brown dwarfs

1. INTRODUCTION

Establishing the masses, radii, effective temperatures, and atmospheric composition and structure of the planets orbiting the A star HR 8799 has been a challenge. Of the four planets (Marois et al. 2008, 2010) directly imaged orbiting the star HR8799, broad wavelength coverage photometric data is available for three, planets b, c, and d (Marois et al. 2008; Currie et al. 2011), and some spectral data is available for one planet, b (Barman et al. 2011a). Efforts to fit the available data with atmosphere and evolution models have produced mixed results. In some cases the best-fitting models predict radii and ages that are at odds with other constraints, such as evolution models and the age of the system. The apparently unusual cloud properties of the planets have also received great attention. Here we present an examination of the properties of HR8799 b, c, and d using all publicly

available data as well as our own evolution and atmosphere models. Our aim is to determine if a set of planet properties can be derived which simultaneously satisfy all observational and theoretical constraints and to ascertain the nature of atmospheric condensate layers in each planet.

We open below with a summary of the model parameters previously derived for these planets. In the remainder of this section we briefly review what is known about the atmospheric evolution of brown dwarfs and discuss the issues that have arisen to date in the study of the HR 8799 planets, particularly regarding the clouds and inferred planet radii. In succeeding sections we explore the nature of clouds in low mass objects more deeply and present model solutions for the mass, effective temperature, and cloud properties of the planets. Unlike previous studies we find that the HR 8799 clouds are similar to those found in field L dwarfs, although they are present to lower effective temperature.

1.1. Masses and Radii of HR 8799 b,c, and d

In the HR 8799 b, c, and d discovery paper, Marois et al. (2008) derived the mass and effective temperature, T_{eff} , of each object in two ways. In the first method they computed the luminosity of each object and compared that to theoretical cooling tracks for young giant planets given the constraint of their estimated age of the primary star. In the second method they fit atmosphere models using the PHOENIX code (Hauschildt et al. 1999) to the available six-band near-infrared photometry to constrain T_{eff} and $\log g$, the two most important tunable parameters of atmosphere models. By comparing the model emergent spectra with the observed photometry and known distance to the target, radii of each planet were derived. Notably only models that included the effects of refractory silicate and iron clouds were consistent with the data. However the radii estimated by this method were far smaller than expected for solar metallicity gas giant planets at such young ages.

Barman et al. (2011a) fit a suite of models to the available photometry (but not the M band (Galicher et al. 2011) data) and H and K band spectra that they obtained for planet b. By comparing the integrated flux from their best fitting model atmosphere to the estimated bolometric luminosity of the planet, they found a small radius for the planet $R \sim 0.75 R_{\text{J}}$.

Galicher et al. (2011), who also relied on the Barman models, fit atmosphere models to the photometry, including the M -band data. They found somewhat higher gravity solutions than Barman et al. (2011a) but also required a very small radius for planet b, approximately 70%–or about one-third the volume–expected from planetary evolution models. The most straightforward interpretation of this discrepancy is that the atmosphere models are not

representative of the actual planetary atmosphere and Barman et al. suggest that higher metallicity models might provide a better fit and give more plausible radii.

Likewise Bowler et al. (2010) selected the model spectra (from among the models of Hubeny & Burrows (2007); Burrows et al. (2006); Allard et al. (2001)) which best fit the available photometry for HR 8799b. Their best fitting spectra were quite warm, with T_{eff} from 1300 to 1700 K and thus they required particularly small radii ($\sim 0.4 R_J$) in order to meet the total luminosity constraint given the photometry available at that time.

In contrast Currie et al. (2011) searched for the best fitting spectral models while requiring that the planet radii were either that predicted by a set of evolution models (Burrows et al. 1997) or were allowed to vary. They found that what they termed to be “standard” brown dwarf cloud models required unphysically small planet radii to fit the data. However their “thick cloud” models could fit the data shortward of $3 \mu\text{m}$ by employing radii that were within about 10% of the usual model prediction. As we note below, however, the “standard” cloud model has itself not been demonstrated to fit cloudy, late L-type dwarfs, thus this exercise does not necessarily imply the HR 8799 planets’ clouds are “non-standard”. Nevertheless they were able to fit much of the photometry with normal planetary radii, although their best fits were not for a single, consistent age for all of the planets.

Finally Madhusudhan et al. (2011) explored a set of models similar to that studied by Currie et al. with yet another cloud model but without the radius constraint. Their best fits are very similar to those of Currie et al. but with somewhat lower T_{eff} .

The characteristics of the planets as derived in the 2011 papers are summarized in Table 1. Not all authors report every parameter so some radii and ages are left blank. Note the diverse set of masses, radii, and effective temperatures derived by the various studies. Despite the variety some trends are clear: planet b consistently is found to have the lowest mass and effective temperature and this planet’s derived radius is almost always at odds with the expectation of evolution models.

1.2. Clouds

1.2.1. *Brown Dwarfs*

As a brown dwarf ages it radiates and cools. When it is warm refractory condensates, including iron and various silicates, form clouds in the visible atmosphere. Over time the clouds become progressively thicker and more opaque, leading to ever redder near-infrared colors. As the dwarf cools the cloud decks are found at higher pressures, deeper in the

atmosphere. Eventually the clouds dissipate. Indeed the first two brown dwarfs to be discovered, GD 165B (Becklin & Zuckerman 1988) and Gl 229B (Nakajima et al. 1995), were ultimately understood to represent these two different end cases: the cloudy L and the clear T dwarfs (see Kirkpatrick (2005) for a review). Understanding the behavior of clouds in substellar atmospheres and how it might vary with gravity has become one of the central thrusts of brown dwarf science.

The earliest models for these objects assumed that the condensates were uniformly distributed vertically throughout the atmosphere (e.g., ?). Later, more sophisticated approaches attempted to model the formation of discrete cloud layers that would result from gravitational settling of grains.

With falling effective temperature, T_{eff} , the base of the primary iron and silicate cloud deck is formed progressively deeper in the atmosphere. Because of grain settling the overlying atmosphere well above the cloud deck loses grain opacity and becomes progressively cooler, thus over time more of the visible atmosphere becomes grain free and cooler. Cooler temperatures favor CH_4 over CO. The removal of the opacity ‘floor’ which the clouds once provided also allows flux in the water ‘window’ regions to escape from deeper in the atmosphere. This leads to a brightening in J band and a blueward color shift. In field brown dwarfs this color change begins around effective temperature $T_{\text{eff}} \sim 1200$ to 1400 K and is complete over a strikingly small effective temperature range of only 100 to 200 K (see Kirkpatrick (2005) for a review). This experience led to the presumption that all objects with effective temperatures below about 1100 K would have blue near-infrared colors, like the field brown dwarfs.

1.2.2. HR 8799 b, c, and d

The first directly imaged low mass companions confounded these expectations from the brown dwarf experience. The companion (Chauvin et al. 2004; ?) to the low mass dwarf 2MASSWJ 1207334-393254 (Gizis (2002), hereafter 2M1207 b) has red infrared colors despite its low luminosity and apparently cool T_{eff} . Likewise the HR 8799 planets have colors reminiscent of hot, cloudy L dwarfs but their bolometric luminosities coupled with a radii from planetary structure calculations imply $T_{\text{eff}} \sim 1000$ K or lower (Marois et al. 2008, 2010).

The red colors, particularly of the HR 8799 planets, spawned a storm of studies investigating the atmospheric structure of the planets. Essentially all of these papers concluded that the planets could be best explained by invoking thick cloud decks. Since this ran counter to expectation, these clouds were deemed “radically enhanced” when compared to

“standard” models (Bowler et al. 2010). Likewise Currie et al. (2011) compared their data to the Burrows et al. (2006) model sequence and concluded (their §5) that the HR 8799 planets have much thicker clouds than “...standard L/T dwarf atmosphere models.” Madhusudhan et al. (2011) state that their fiducial models “...have been shown to provide good fits to observations of L and T dwarfs (Burrows et al. 2006)”. They then find that much cloudier models are required to fit the imaged exoplanets and thus conclude that the cloud properties must be highly discrepant from those of the field L dwarfs.

Such conclusions, however, overlook that the study of L dwarf atmospheres is still in its youth. Cloudy atmospheres of all kinds are challenging to model and the L dwarfs have proven to be no exception. Thus whether or not the HR 8799 planets have unusual clouds depends on the point of reference. Indeed while most published models of brown dwarfs are able to reproduce the spectra of cloudy, early L-type dwarfs and cloudless T dwarfs, the latest, reddest—and presumably cloudiest—L dwarfs have been a challenge. Burrows et al. (2006), for example, compare their model predictions to photometry of L and T dwarfs. They find that their models do not reproduce the colors of the latest L dwarfs as the models are too blue (see their figure 17) implying that they lack sufficient clouds. Burrows et al. (2006) also present comparisons of their models to L dwarf spectra, however the comparisons are only to an L1 and an L5 dwarf. There are no comparisons to very cloudy late L dwarf spectra in the paper so the fidelity of their model under such conditions cannot be judged. For these reasons a comparison of the cloudy HR 8799 planets to the supposedly “standard” L dwarf models, such as presented by Madhusudhan et al. (2011) and Currie et al. (2011), begs the question if the HR 8799 planets are really all that different from the cloudiest late L dwarfs.

Some atmosphere and evolution models, however, have been compared against the spectra and colors of latest L dwarfs. In Cushing et al. (2008) and Stephens et al. (2009) we compared our group’s models to observed far-red to mid-infrared spectra of L and T dwarfs, including L dwarfs with IR spectral types as late as L9. We found that the models with our usual cloud prescription fit well, but not perfectly, the spectra of L dwarfs of all spectral classes, including the latest field L dwarfs. In Saumon & Marley (2008) we presented a model of brown dwarf evolution that well reproduced the usual near-infrared color magnitude diagram of L and T dwarfs, including the reddest L dwarfs. Here we apply this same model set to the HR 8799 planet observations to understand the objects.

1.3. Chemical Mixing

Shortly after the discovery of Gl 229B, Fegley & Lodders (1996) predicted that—as in Jupiter—vertical mixing might cause CO to be overabundant compared to CH₄ in this object. This was promptly confirmed by the detection of CO absorption at 4.6 μm by Noll et al. (1997) and Oppenheimer et al. (1998). The overabundance is caused by the slow conversions of CO to CH₄ relative to convective transport timescales.

An obvious mechanism for vertical mixing in an atmosphere is convection. Brown dwarf atmospheres are convective at depth where the mixing time scale is short (minutes). The overlying radiative zone is usually considered quiescent but a variety of processes can cause vertical mixing, albeit on much longer time scales. Since the conversion time scales for CO → CH₄ and N₂ → NH₃ range from seconds (at $T \sim 3000$ K) to many Hubble times (for $T < 1000$ K), even very slow mixing in the radiative zone can drive the chemistry of carbon and nitrogen out of equilibrium. From this basic consideration, it appears that departures from equilibrium are inevitable in the atmospheres of cool brown dwarfs and indeed the phenomenon is well established (e.g., Saumon et al. 2000; Geballe et al. 2001, 2009; Mainzer et al. 2007; Saumon et al. 2006; Stephens et al. 2009).

2. Gravity, Refractory Clouds and the L/T Transition

Probably need some text here.

2.1. Nature of the Transition

Two main underlying causes of the loss in cloud opacity at the L to T transition have been suggested. In one view the atmospheric dynamical state changes, resulting in larger particle sizes that more rapidly ‘rain out’ of the atmosphere, leading to a sudden clearing or collapse of the cloud (Knapp et al. 2004; Tsuji & Nakajima 2003; Tsuji et al. 2004). This view is supported by fits of spectra to model spectra (Saumon & Marley 2008) computed with the Ackerman & Marley (2001) cloud model. In that formalism, a tunable parameter, f_{sed} controls cloud particle sizes and optical depth. Larger f_{sed} yields larger particles along with physically and optically thinner clouds. Cushing et al. (2008) and Stephens et al. (2009) have demonstrated that progressively later dwarfs (L9 to T4) can be fit by increasing f_{sed} across the transition. A variation on this hypothesis is that a cloud particle size change is responsible for the transition (Burrows et al. 2006).

The second view is inspired by thermal infrared images of the atmospheres of Jupiter and Saturn at $\sim 5 \mu\text{m}$ (e.g. Westphal 1969; Westphal et al. 1974; Orton et al. 1996; Baines et al. 2005). Gaseous opacity is low at this wavelength and the clouds stand out as dark, mottled features against a bright background of flux emitted from deeper, warmer levels in the atmosphere. Such images of both Jupiter and Saturn clearly show that the global cloud decks are not homogenous, but rather are quite patchy. Ackerman & Marley (2001), Burgasser et al. (2002), and Marley et al. (2010) have suggested that the arrival of holes in brown dwarf clouds, perhaps due to the clouds passing through a dynamical boundary in the atmosphere, might also be responsible for the L to T transition. This view is supported by the discovery of L-T transition dwarfs that vary in brightness with time with relatively large near-infrared amplitudes (Artigau et al. 2009; Radigan et al. 2011). Indeed Radigan (in prep) has found in a survey of about 60 L and T type brown dwarfs that the most variable dwarfs are the early T’s, which are right in the middle of the $J - K$ color change.

Modern thermal evolution models for the cooling of brown dwarfs have to impose some arbitrary mechanism, such as varying sedimentation efficiency or the imposition of cloud holes, by which the thick clouds in the late L dwarfs dissipate. A uniform cloud layer that simply sinks with falling T_{eff} as the atmosphere cools turns to the blue much more slowly than is observed. Application of such a transition mechanism to reliably reproduce the colors and spectra of late L and early T dwarfs (e.g., near-IR color-magnitude diagrams) led to the expectation that the normal behavior for cooling brown dwarfs—or extrasolar giant planets—is to turn to the blue at around 1300 K.

However there have been indications that such a narrative is too simple and that gravity plays a role as well. Two brown dwarf companions to young main sequence stars were found to have unexpectedly cool effective temperatures for their L-T transition spectral types by Metchev & Hillenbrand (2006) and Luhman et al. (2007). The analysis of Luhman et al. of the T dwarf HN Peg B was further supported by additional modeling presented in Leggett et al. (2008). Dupuy et al. (2009) presented evidence a gravity dependent transition T_{eff} on the basis of a dynamical mass determination of an M8 + L7 binary. Stephens et al. (2009) fit the model spectra of Marley et al. (2002) to L and T dwarf spectra and found that L dwarf cloud clearing (as characterized by large f_{sed}) occurs at $T_{\text{eff}} \sim 1300 \text{ K}$ for $\log g = 5.0$ and at $\sim 1100 \text{ K}$ for $\log g = 4.5$, although the sample size was admittedly small (Figure 1). Nevertheless such an association predicts a cooler transition temperature at even lower gravity.

2.2. Clouds at Low Gravity

Thus even if the directly imaged planets are not considered, there is already considerable evidence that the cloud clearing associated with the L to T transition occurs at lower effective temperatures in lower gravity objects than in high gravity ones. To understand what lies behind this trend it is necessary to consider three separate questions. First, where does the optically-thick portion of the cloud lie in the atmosphere relative to the photosphere? An optically-thick cloud lying well below the photosphere will be essentially invisible whereas the same cloud lying higher in the atmosphere would be easily detected. Second, how does the optical depth of the cloud vary with gravity? This is a complex problem involving the pressure of the cloud base and the particle size distribution. Third, how does the mechanism by which clouds dissipate vary with gravity? For example, do holes form at a different effective temperature in different gravity objects? In this section we consider only the first two questions and defer the third question to the discussion section.

To address the first question we need to understand how atmospheric temperature T varies with pressure P as a function of gravity. For a fixed effective temperature, a lower gravity atmosphere is warmer at a fixed pressure level than a higher gravity one. This is because more molecules—and thus greater opacity—overlie a given pressure level at lower gravity. Figure 2 provides an example using our model profiles. The vapor pressure curve for condensation also always has a slight negative slope on such figures. Since at equilibrium condensation begins at the intersection of the vapor pressure and thermal profiles, the cloud base occurs at lower pressure (higher in the atmosphere) in a low gravity object than a high gravity one.

As objects cool with time (at essentially fixed gravity) clouds will persist at lower pressure and remain visible to cooler effective temperatures in lower gravity objects than higher gravity ones. For example in Figure 2 the lowest gravity model shown at $T_{\text{eff}} = 900$ K is hotter at all pressures greater than a few hundred millibar than a high gravity $T_{\text{eff}} = 1300$ K object. This is likely why early fits to only the relative photometry for the HR 8799 planets yielded unexpectedly high effective temperatures (Marois et al. 2008).

To address the second question we must understand how the cloud column optical depth varies with gravity. This depends both on the amount of condensible material available in the atmosphere available to form clouds and the cloud particle size. From basic scaling laws and mass balance Marley (2000) derived an expression for the wavelength-dependent total column optical depth τ_λ of a cloud in a hydrostatic atmosphere, assuming Mie theory,

$$\tau_\lambda = 75\epsilon Q_\lambda(r_c)\varphi\left(\frac{P_{cl}}{1 \text{ bar}}\right)\left(\frac{10^5 \text{ cm s}^{-2}}{g}\right)\left(\frac{1 \mu\text{m}}{r_c}\right)\left(\frac{1.0 \text{ g cm}^{-3}}{\rho_c}\right). \quad (1)$$

Here P_{cl} , r_c and ρ_c refer to the pressure at the cloud base and the condensate mean radius and density (see also Eq. 18 of Ackerman & Marley (2001)). φ is the product of the condensing species number mixing ratio and the ratio of the mean molecular weight of the condensate to that of the background gas. The expression assumes that some fraction ϵ of the available mass above the cloud base forms particles which can be described by Mie theory as having extinction cross section Q_λ . Ackerman & Marley (2001) also estimate the column optical depth of a cloud with a similar result. Generalizing their Eq. 16,

$$\tau_\lambda \propto \frac{P_{cl}}{gr_{\text{eff}}(1 + f_{\text{sed}})}. \quad (2)$$

Where r_{eff} is the mean (area-weighted) droplet size and f_{sed} is the sedimentation efficiency.

Both Equations (1) and (2) hold that all else—including particle sizes—being equal, we expect $\tau \propto P_{cl}/g$, just because the column mass above a fixed pressure level is higher at low gravity and there is more material to condense. Any cloud model which self-consistently computes the column mass of condensed material should reproduce this result. As we argued above, however, the cloud base is at lower pressure in lower gravity objects, roughly $P_{cl} \propto g$, thus predicting that the cloud τ would be roughly constant with changing gravity. This is not exactly true since there is a slope to the vapor pressure equilibrium curve and thus the actual variation is somewhat weaker, but we the effects of gravity and the cloud base pressure alone do not strongly influence cloud column optical depth.

The second component affecting the column cloud opacity is the particle size. While a cloud model is required for rigorous particle size computation, we can examine the scaling of size with gravity. At lower gravity particle fall speeds are reduced which reduces the downward mass flux carried by condensates of a given size. Since fall speed is proportional to r_c^2 while the mass flux is proportional to r_c^3 , a slight increase in particle size can produce the same mass balance in the atmosphere at lower gravity, and thus r_c is expected to increase relatively slowly with decreasing g . Indeed the Ackerman & Marley (2001) model suggests $r_c \propto (f_{\text{sed}}/g)^{1/2}$, although the actual dependence is more complex as it depends upon an integral over the size distribution. Tests with the complete cloud model coupled to our atmosphere code predict about a factor of 4 increase in cloud particle radius (25 to 100 μm) as gravity decreases by an order of magnitude from 300 to 30 m s^{-2} , a slightly faster increase than $\frac{1}{\sqrt{10}}$ but similar to the variation seen in Figure 6 of Ackerman & Marley (2001). Returning to Eq. (1) and combining with the scaling discussed above thus suggests that all else being equal we expect cloud $\tau \propto \sqrt{g}$.

Figure 3 illustrates all of these effects in model cloud profiles calculated for three atmosphere models with varying g and T_{eff} (the justification for the specific parameter choices is given in the discussion section). The atmospheric gravity spans two orders of magnitude

while the effective temperature varies from 1200 to 1000 K from the warmest to coolest object. As expected the cloud particle size indeed varies inversely with gravity while the cloud base pressure decreases with gravity. The choice in the plot of a cooler T_{eff} for the lowest gravity object counteracts what would otherwise be an even greater difference in the cloud base pressure. The net result is that the total column optical depth for the silicate cloud in all three objects is very similar, $\tau \sim 10$. *Thus a cooler, low gravity object has a cloud with a column optical depth that is almost indistinguishable from that of a warmer, more massive object.*

The thicker portion of the lines denoting cloud column optical depth signify the regions in the atmosphere where the brightness temperature is equal to the local temperature. In other words the thick line represents the near-infrared photosphere. In all three cases there is substantial cloud optical depth ($\tau_{\text{col}} > 0.1$) in the deeper atmospheric regions from which flux emerges in the near-infrared. As a result the impact of the cloud modeled in all three objects is comparable despite the two order of magnitude difference in gravity even though the lowest gravity model is notably cooler—by 200 K—than the highest gravity one.

We thus conclude that the net effect of all of these terms is to produce clouds in lower gravity objects with optical depths and physical locations relative to the photosphere in the atmosphere comparable to clouds in objects with higher gravity and higher effective temperature. Despite these scaling arguments, of course, only a complete self-consistent model calculation can truly test the hypothesis.

3. Modeling Approach

To model the atmospheres and evolution of exoplanets we apply our usual modeling approach which we briefly summarize in this section. We stress that the fidelity of model fits in previous applications of our method to both cloudy and clear atmosphere brown dwarfs (Marley et al. 1996, 2002; Burrows et al. 1997; Roellig et al. 2004; Saumon et al. 2006, 2007; Leggett et al. 2007a,b; Mainzer et al. 2007; Blake et al. 2007; Cushing et al. 2008; Geballe et al. 2009; Stephens et al. 2009) validates our overall approach and provides a basis of comparison to the directly imaged planet analysis. Indeed the model has successfully been applied not only to brown dwarfs, but Uranus (Marley & McKay 1999) and Titan (McKay et al. 1989) as well.

3.1. Atmosphere and Cloud Models

The atmosphere models are described in McKay et al. (1989); Marley et al. (1996); Burrows et al. (1997); Marley & McKay (1999); Marley et al. (2002); Saumon & Marley (2008). Briefly we solve for a radiative-convective equilibrium thermal profile that carries thermal flux given by σT_{eff}^4 given a specified gravity and atmospheric composition. The thermal radiative transfer follows the source function technique of Toon et al. (1989) allowing inclusion of arbitrary Mie scattering particles in the opacity of each layer. Our opacity database includes all important absorbers and is described in Freedman et al. (2008).

There are, however, two particularly important updates to our opacity database since Freedman et al. (2008). First we use a new molecular opacity database for ammonia (Yurchenko et al. 2011). Secondly we have replaced our previous treatment of pressure-induced opacity arising from collisions of H_2 molecules with H_2 and He with a new calculation. The new opacity is discussed in Frommhold et al. (2010) and the impact on our model spectra and photometry in general is discussed in Saumon et al. (2012).

The abundances of molecular, atomic, and ionic species are computed for chemical equilibrium as a function of temperature, pressure, and metallicity following Fegley & Lodders (1994, 1996); Lodders (1999); Lodders & Fegley (2002); Lodders (2003); Lodders & Fegley (2006) assuming the elemental abundances of Lodders (2003). In this paper we explore only solar composition models.

For cloud modeling we employ the approach of Ackerman & Marley (2001) which parameterizes the relative importance of sedimentation relative to upwards mixing of cloud particles through an efficiency factor, f_{sed} . Large values of f_{sed} correspond to rapid particle growth and large mean particle sizes. Under such conditions condensates quickly fall out of the atmosphere, leading to physically and optically thin clouds. In the case of small f_{sed} particles grow more slowly resulting in a larger atmospheric condensate load and thicker clouds. Both our cloud model and chemical equilibrium calculations are fully coupled with the radiative transfer and the (P, T) structure of the model during the calculation of a model so that they are fully consistent when convergence is obtained.

We note in passing that the cloud models employed in previous studies of the HR 8799 planets have been *ad hoc*, as straightforwardly discussed in those papers. Particle sizes, cloud heights, and other cloud properties are fixed at given values while gravity, T_{eff} , and other model parameters are varied. We stress that our approach is distinct since in each case we compute a self-consistent set of cloud properties given a specific modeling approach, the Ackerman & Marley cloud.

The coupled cloud and atmosphere models have been widely compared to spectra and

photometry of L and T dwarfs in the publications cited in the introduction to this section. We emphasize in particular that Cushing et al. (2008) and Stephens et al. (2009) show generally excellent fits between our model spectra and observations of cloudy L dwarfs. The near-infrared colors of brown dwarfs are quite sensitive to the choice of f_{sed} , a point we will return to.

3.2. Evolution Model

Our evolution model is described in Saumon & Marley (2008). In fitting the HR 8799 data, we use the sequence computed with a surface boundary condition extracted from our cloudy model atmospheres with $f_{\text{sed}} = 2$. As we will see below, our best fits show that all three planets are cloudy with $f_{\text{sed}} = 2$, which justifies this choice of evolution *a posteriori*. As the three planets appear to have significant cloud decks (as will be confirmed below), it is not necessary to use evolution sequences that take into account the transition explicitly (e.g. Saumon & Marley (2008)) in this comparison with models. Nevertheless, we will explore the effects of a gravity-dependent transition between cloudy and cloudless atmospheres in section YYY as this is a topic of growing interest.

4. Application to HR 8799 Planets

4.1. Constraints on the HR 8799 System Properties

A number of the properties of the HR 8799 system as a whole help to constrain the properties of the individual planets. Of foremost importance of course is the age of the primary star. Older ages of the primary star require greater planetary masses to provide a fixed observed luminosity while younger ages allow lower masses. The massive dust disk found outside of the orbit of the most distant planet, HR 8799 b, constrains the mass of that planet since a very massive planet would disrupt the disk. Finally dynamical models of the planetary orbits can point to systems that are or are not stable over the age of the system. All of these topics have been discussed extensively in the literature so here we briefly summarize the current state of affairs. A more thorough review can be found in Sudol & Haghighipour (2012).

Since the discovery of the first three planets, the age of HR 8799 has been a topic of extensive discussion. As summarized initially by the discoverers, most indicators suggest a young age of 30 to 60 Myr (Marois et al. 2008). However as a λ Boo-type star with an unusual atmospheric and uncertain internal composition the typical age metrics are somewhat more

in doubt than usual. Moya et al. (2010) review the various estimates of the age of the star prior to 2010 and argue that most of the applied metrics, including color and position on the HR diagram, are not definitive. Most recently Zuckerman et al. (2011) conclude that the Galactic space motion of HR 8799 is very similar to that of the 30 Myr old Columba association and suggest that it is a member of that group. They also argue that the $B - V$ color of HR 8799 in comparison to Pleiades A stars also supports a young age, although the unusual composition hampers such an argument. Perhaps the fairest summary of the situation to date would be that most traditional indicators support a young age for the primary, but that no single indicator is entirely definitive on its own.

One indicator that the age could be much greater than usually assumed is discussed by Moya et al. (2010). Those authors use the γ Doradus g-mode pulsations of the star to place an independent constraint on the stellar age. Their analysis is dependent upon the rotation rate of the star and consequently the unknown inclination angle and thus is also uncertain. Nevertheless they find model solutions that match the observed properties of the star in which the stellar age can plausibly be in excess of 100 Myr and in some cases as large as 1 Gyr or more. They state that their analysis is most uncertain for inclination angles in the range of 18 to 36°, which corresponds to the likely inclination supported by observations of the surrounding dust belt (see below). Thus stellar seismology provides an intriguing, but likewise still uncertain constraint.

The dust disk encircling the orbits of the HR 8799 planets can in principle provide several useful constraints on the planetary masses and orbits. First the inclination of the disk has bearing on the computed orbital stability of the companions (Fabrycky & Murray-Clay 2010) if we assume the disk is coplanar with the planetary orbits. If the rotation axis of the star is perpendicular to the disk the inclination has a bearing on the stellar age since the seismological analysis in turn depends upon its inclination to our line of sight (Moya et al. 2010). Hughes et al. (2011) discuss a variety of lines of evidence that bear on the inclination, i , of the HR 8799 dust disk. While they conclude that inclinations near 20° are most likely, the available data cannot rule out a face-on ($i = 0^\circ$) configuration. Finally an additional important constraint on the mass of HR 8799 b could be obtained if it is responsible for truncating the inner edge of the dust disk. An inner edge at 150 AU is consistent with available data (Su et al. 2009) and this permits HR 8799 b to have a mass as large as 20 M_J (Fabrycky & Murray-Clay 2010). It is worth noting, however, that this limit depends upon the model-dependent inner edge of the disk and the dynamical simulations.

Finally dynamical simulations of the planetary orbits constrained by the available astrometric data can provide planetary mass limits. In the most thorough study to date Fabrycky & Murray-Clay (2010) found that if planets c and d were in a 2:1 mean-motion resonance

their masses could be no larger than about $10 M_J$. However if there were a double resonance in which c, d, and b participated in a “double 2:1” or 1:2:4 resonance (originally identified by Goździewski & Migaszewski (2009)) then masses as large as $20 M_J$ are permitted and such systems are stable for 160 Myr (Fabrycky & Murray-Clay 2010). Such a resonance was found to be consistent with the limited baseline of astrometric data. Very recently, however, HR 8799 b,c, and d were identified in an archived HST image taken in 1998 (Soummer et al. 2011). The new data continue to allow the possibility of the 1:2:4 mean motion resonance, a solution which implies a moderate inclination ($i = 28^\circ$) for the system. New dynamical models that include both this new astrometric data and the innermost e planet are now required to fully evaluate the system’s stability. Sudol & Haghighipour (2012) studied such a system with masses of 7, 10, 10, and $10 M_J$. They generally found system lifetimes shorter than 50 Myr for such large masses but at least one system was found to be stable for almost 160 Myr.

Taken as a whole the age of the system and the available astrometric data and dynamical models are consistent with a relatively young age (30 to 60 Myr) and low masses for the planets (below $10 M_J$). However the possibility of an older system age, as allowed by the asteroseismology, and higher planet masses, as permitted if the planets are in resonance, cannot be fully ruled out. Given this background we now consider the planetary atmosphere models.

4.2. Data Sources

The available photometric data for each planet is summarized in Table 2 and shown on Figures 3, 4, and 5. In addition for planet b we employ H and K band spectra as tabulated in Barman et al. (2011a). Below we summarize the sources of the photometry.

4.2.1. *z*-band

The *z*-band photometry is from Currie et al. (2011) and was obtained with the Infrared Camera and Spectrograph (IRCS; Tokunaga et al. (1998)) on the Subaru Telescope. The filter profile was kindly provided by Tae-Soo Pyo in image form and then was digitized using PlotDigitizer. No atmospheric absorption was included because the filter sits in a window that is nearly perfectly transparent.

4.2.2. *J-band*

The *J*-band data was taken from Marois et al. (2008) and Currie et al. (2011). The former observations were done with the Near-Infrared Camera (NIRC2) on Keck II which uses a MKO-NIR J band filter. We used the filter transmission profile from Tokunaga et al. (2002) and an atmospheric transmission curve computed using ATRAN at an airmass of 1, with a precipitable water vapor of 2 mm. The former observations were obtained with the Infrared Camera and Spectrograph (IRCS; Tokunaga et al. (1998)) on the Subaru Telescope which also uses a MKO-NIR J band filter.

4.2.3. *H- and K_s -bands*

The *H*-band and K_s -band data were taken from Marois et al. (2008). The observations were done with the Near-Infrared Camera (NIRC2) on Keck II which uses MKO-NIR filters. We used the filter transmission profile from Tokunaga et al. (2002) and an atmospheric transmission curve computed using ATRAN at an airmass of 1, with a precipitable water vapor of 2 mm.

4.2.4. *[3.3]-band*

The [3.3]-band data was taken from (Currie et al. 2011). The observations were done with the Clio camera at the MMT Telescope. The filter is non standard and has a central wavelength of $3.3\ \mu\text{m}$, and half-power points of 3.10 and $3.5\ \mu\text{m}$. The filter transmission profile was provided by Phil Hinz. **Apparently I haven't added the atmospheric transmission, so I need to check into that!**

4.2.5. *L'-band*

The *L'*-band data was taken from Currie et al. (2011). The filter is the *L'* filter in the MKO-NIR system so we used the filter transmission profile from Tokunaga et al. (2002) and an atmospheric transmission curve computed using ATRAN at an airmass of 1, with a precipitable water vapor of 2 mm.

4.2.6. M' -band

The M-band photometry of Galicher et al. (2011) was obtained using the Near-Infrared Camera (NIRC2) on Keck II. This filter profile is the same as the M' band of the MKO-NIR system. We therefore used the filter transmission profile from Tokunaga et al. (2002) and an atmospheric transmission curve computed using ATRAN at an airmass of 1, with a precipitable water vapor of 2 mm.

4.3. Fitting Method

In order to determine the atmospheric properties of the HR 8799 planets, we compared the observed photometry to synthetic spectra generated from our model atmospheres. We used a grid of solar metallicity models with the following parameters: $T_{\text{eff}} = 800\text{--}1300$ K in steps of 50 K, $\log g = 3.5\text{--}5.5$ in steps of 0.25 dex, $f_{\text{sed}} = 1, 2$, and eddy mixing coefficient $K_{\text{zz}} = 0, 10^4 \text{ cm}^2 \text{ s}^{-1}$. We identify the best fitting model and estimate the atmospheric parameters of the planets following the technique described in Cushing et al. (2012, in prep). In brief, we use Bayes' theorem to derive the joint posterior probability distribution of the atmospheric parameters given the data $P(T_{\text{eff}}, \log g, f_{\text{sed}}, K_{\text{zz}}|\mathbf{f})$, where \mathbf{f} represents a vector of the flux density values (or upper limits) in each of the bandpasses. The best fitting model is that one with the largest posterior probability.

Estimates and uncertainties for each of the atmospheric parameters can also be derived by first marginalizing over the other parameters and then computing the mean and standard deviation of the resulting distribution. For example, the posterior distribution of T_{eff} is given by,

$$P(T_{\text{eff}}|\mathbf{f}) = \int P(T_{\text{eff}}, \log g, f_{\text{sed}}, K_{\text{zz}}|\mathbf{f}) d \log g df_{\text{sed}} dK_{\text{zz}}$$

Since $(T_{\text{eff}}, \log g)$ values can be mapped directly to (M, R) values using evolutionary models, we can also construct marginalized distribution for M and R . Figure 8 shows the distributions of T_{eff} , $\log g$, and M for each of the planets and Table II lists estimates of the parameters and associated uncertainties.

Finally note that we chose to use a Bayesian formalism rather than minimizing χ^2 (as is more common) because 1) we can marginalize over nuisance model parameters such as the distance and radii of the brown dwarfs, and 2) we can incorporate upper limits using the formalism described in Isobe et al. (1986).

4.4. Best Fits

In this section we discuss the individual best fits to each planet. Figures 4, 5, and 6 compare the fits to the observed spectra and photometry. Figures 7 a, b, and c show contours in the $\log g - T_{\text{eff}}$ plane of the best fitting models. For each object the contours enclose the range of models which fit the data within 1, 2, and 3- σ . In these figures evolution tracks for planets and brown dwarfs of various masses are shown. The objects evolve from right to left across the figures as they cool over time. Isochrones for a few ages are shown as well. The kinks arise from deuterium burning. Thus in some cases at a fixed age a given T_{eff} can correspond to three different possible masses (e.g., a 1150 K object at 160 Myr). Also shown are contours of constant L_{bol} .

The best fitting parameters are also shown in Figure 8 as histograms of fit quality for $\log g$ and T_{eff} . The histograms are projections of the contours shown in Figure 7 onto these two orthogonal axes. The mean of the fit and the size of the standard deviation is indicated in each panel and also illustrated by the solid and dashed vertical lines. The third column of histograms depicts the same information as the first two, but for the mass corresponding to each $(T_{\text{eff}}, \log g)$ pair, as computed by the evolution model.

We discuss each set of fits for each planet in turn below.

4.4.1. HR 8799 b

HR 8799 b is the only one of the three planets considered here for which there is spectroscopic data and our results are sensitive to whether or not this data is included in our fit. Contours which show the locus of the best fitting models for both datasets are shown in Figure 7a. When only the photometric data is fit high masses around $\sim 27 M_{\text{J}}$ are favored. Inclusion of the spectral data dramatically lowers the best fitting mass to $\sim 3 M_{\text{J}}$. Both sets of models strongly favor $T_{\text{eff}} = 1000 \text{ K}$ and $f_{\text{sed}} = 2$. The models which best fit the photometry alone, the spectroscopy alone, and the combination of the two are illustrated in Figure 4.

The reason the derived gravity depend so strongly on the H and K spectra is that the shape of the emergent flux—and not just the total flux in a given band—contains information about the gravity. The famous “triangular” H band shape as an indicator of low gravity results from the interplay of molecular hydrogen pressure-induced opacity and a sawtooth-shaped water opacity. At high pressures the continuum hydrogen opacity tends to fill in the opacity trough at the minimum of the water opacity in H band. Since the photosphere of lower gravity objects is at lower pressures, the H_2 opacity is somewhat less important

allowing the angular shape of the water opacity to more strongly control the emergent flux. The models which best reproduce this effect are indeed the low gravity models, as seen in the middle panel of Figure 4.

The overall best fitting model fits the Y, J, [3.3], and M' photometry to within 1σ . The model is slightly too dim at L' . We note in particular the fit to the 3.3- μm datapoint within 1σ , something that other models have struggled with (e.g., Currie et al. 2011; Madhusudhan et al. 2011). The shape of H band is fairly well reproduced but not K band for which the model is about 20% too faint at $\lambda > 2.1\mu\text{m}$. The overall quality of the fit is comparable to or better than other fits in the literature. However unlike most of the previous models the radius, effective temperature, and gravity are all self consistent. Both sets of solutions, however, are inconsistent with the accepted age of the the star. The lower mass solutions would imply very young ages for the planet, well below 30 Myr. Conversely the higher mass range implies ages in excess of about 300 Myr.

4.4.2. HR 8799 c

For planet c there is no available spectroscopy and we fit only to the photometry. The formal best fitting solution yields $T_{\text{eff}} = 1000 \pm 75$ K and $\log g = 4.67 \pm 0.26$ for a mass of $18 \pm 8 M_{\text{J}}$. However in both the contour diagram (Figure 7b) and the histogram (Figure 8) we again find two islands or clusters of acceptable fits, one at higher gravity and effective temperature, and one with lower values for both. The high mass solution lies at masses in excess of $20 M_{\text{J}}$ and $T_{\text{eff}} \sim 1100$ K. Such models are consistent only with ages around 300 My, in excess of the preferred age range for the primary and the dynamical constraints. The second ‘island’ of acceptable fits lies at $\log g \sim 4.25$ and $T_{\text{eff}} \sim 950$ K. Figure 5 illustrates the spectra for the best fitting model from each case. The lower mass, younger model has $\log g = 4.25$, $f_{\text{sed}} = 2$, and $\log K_{\text{zz}} = 4$, implying $M = 10 M_{\text{J}}$ which is consistent with the dynamical mass constraint and represents our preferred solution. The age predicted by the evolution of these models is about 160 Myr, consistent with the astroseismological age constraint but not the generally favored range of 30 to 60 Myr.

The overall quality of the fits is somewhat poorer than for HR 8799 b, although most photometric points are fit within $2\text{-}\sigma$. The low mass model varies most significantly from the data at L' . The lower gravity solutions differ from the high gravity ones most prominently in the red side of K band and at 3 to 4 μm . K band spectroscopy has the potential to clarify between these two cases.

4.4.3. *HR 8799 d*

Because of larger observational error bars, the model fits for the innermost of the three planets considered here are the most uncertain. As seen in Figure 7c the best fitting models allow masses ranging from 5 to 60 M_J and T_{eff} between 900 and 1200 K. However the very best fitting models favor solutions with $\log g$ around 4.25 to 4.50 and $T_{\text{eff}} = 1000$ K yielding a mass of 10 M_J . As with planet c such solutions are consistent with the dynamical constraint but not the age constraint. The best fitting spectrum is shown in Figure 6.

5. Discussion

5.1. Implied Masses and Ages

To summarize our findings from the previous section, each of the three planets considered presents a different challenge to characterize. Planet d is least well constrained and consequently its properties are highly uncertain. Nevertheless the best fitting model solutions lie in the range of 10 to 28 M_J and an age of 160 to 500 Myr. For planet c many of the best fitting models are consistent with implausibly large masses, in excess of 20 M_J . However a number of models, including the second and third individual best fitting models, are consistent with masses near 10 M_J and an age of 160 Myr. Thus we find that a consistent solution can be found for planets c and d in which both are 10 M_J and 160 Myr old. This is essentially the solution favored by the discovery paper (Marois et al. 2008) and is within the ranges of favored solutions presented by Currie et al. (2011) and Madhusudhan et al. (2011). However we differ from most of these previous studies in our finding that the radii of these planets are fully consistent with that expected for those masses and ages. Unusual radii are not required. This age is greater than the range of ages typically quoted for the primary star of 30 to 60 Myr, although it is within the range permitted by the asteroseismology.

Planet b, however, presents something of a conundrum. Fits to the photometry alone favor relatively high masses and large ages, in excess of 20 M_J and 300 Myr respectively. Both are at odds with the known constraints. Including the H and K band spectra brings the best fit down to much lower masses and young ages, below 5 M_J and 20 Myr. In this case the age is too young given conventional evolution models and the age of the primary star. However all of the fits for this planet strongly favor $T_{\text{eff}} = 1000 \pm 25$ K so we regard this result with the greatest confidence. This effective temperature is consistent with that favored by Barman et al. (2011a) and Currie et al. (2011) but is substantially warmer than that found by Madhusudhan et al. (2011).

A likely explanation for the difficulty in fitting this object is that one of the assumptions of the modeling is incorrect. Barman et al. (2011a) speculate that a super-solar atmospheric abundance of heavy elements might explain the departures of the data from the models. Indeed all of the atmospheres of solar system giant planets are enhanced over solar abundance with a trend that the enhancement is greater at lower masses. For example Saturn’s atmosphere is enhanced in methane by about a factor of ten while Jupiter is only a factor of about three (see Marley et al. (2007) for a review). The available data on exoplanet masses and radii suggest that lower mass planets are more heavily enriched in heavy elements than higher mass planets (Miller & Fortney 2011). If the mass of HR 8799b is intermediate between our two sets of best fits, for example with a mass near 6 or 7 M_J , as favored by the discovery paper, and if atmospheric abundance trends are similar in the HR 8799 system to our own, then it may not be surprising if the atmospheric abundances differ in b than in c and d. We will consider non-solar abundance atmosphere models in a future paper.

5.2. Bolometric Luminosities

The distance to HR 8799 has been measured as 39 ± 1.0 pc (van Leeuwen 2007) and thus the bolometric luminosities of each planet can be computed from the observed photometry. In the discovery paper Marois et al. (2008) compare the photometry available at that time to models and brown dwarf spectra and report $\log L_{\text{obs}}/L_{\odot} = -5.1 \pm 0.1$ for planet b and -4.7 ± 0.1 for c and d and these are the values still commonly cited. Comparison of model fluxes to these values has led to the concerns about object radii as discussed in Section 1.1.

However since the models as presented in Marois et al. (2008) did not well reproduce the photometry, their bolometric luminosities may be more uncertain than stated. For example in Figure 7 the best fit to the photometry data alone for planet b gives a bolometric luminosity in good agreement with the standard value. However fits to the photometry plus spectra with a model radius drawn from the appropriate evolution model give a substantially higher value of $\log L_{\text{obs}}/L_{\odot} = -4.7$. As seen in Figure 4 such a model fits all of the available photometry within 1σ except for the L' band point where the model is about 1.8σ too faint. Since such a model is clearly plausible, we conclude that the stated luminosity error in Marois et al. (2008) is too small. Based on the solution presented in Figure 8, we estimate the luminosity for planet b to reside in the range $\log L_{\text{obs}}/L_{\odot} = -5.1$ to -4.8 applying only the photometry or -4.7 to -4.6 when both the photometry and spectra are applied. The ranges for planets c and d are -5 to -4.7 and -5 to -4.6 respectively.

5.3. Cloud Properties

Although there is a dispersion in the best fitting $\log g$ and T_{eff} , essentially all of the acceptable fits require a cloud sedimentation efficiency of $f_{\text{sed}} = 2$. As shown in Figure 1 this value is typical of the best fitting parameters for most field L dwarfs we have previously studied (Cushing et al. 2008; Stephens et al. 2009). The persistence of clouds to lower effective temperatures at low gravity is also apparent from this figure. By 1000 K most field dwarfs with $\log g \geq 5$ have already progressed to $f_{\text{sed}} \geq 4$ whereas clouds persist much more commonly among lower gravity objects down to 1000 K. By very cool effective temperatures, however, the silicate and iron clouds have certainly departed from view as demonstrated by the one $\log g = 4$, $T_{\text{eff}} \sim 500$ K object (ULAS J133553.45+113005.2, (Burningham et al. 2008; Leggett et al. 2009)).

As Figure 1 attests, the cloud in planets b, c, and d are unusual not so much for their global characteristics (the same cloud model that describes L dwarf clouds fits them as well), but rather for their persistence. For fixed $f_{\text{sed}} = 2$ there are three field objects with $T_{\text{eff}} \leq 1200$ K. These objects are 2MASS 0825+21, SDSS 0857+57, and SDSS J151643.01+305344.4 (hereafter SDSS 1516+30). Their infrared spectral types are L6, L8, and T0.5 and the first two are both redder in $J - K$ than is typical for those spectral types (Stephens et al. 2009).

Figure 2 compares some of the silicate cloud properties of the best-fitting, low gravity planet b model with the models for the field L6 and T0.5 objects. As expected from the discussion in Section 2.2, the lower gravity model is marked by a larger particle size than the higher gravity models, and the column optical depth of the silicate cloud in all three objects ends up being very similar. More importantly the range of cloud optical depths that lie in the near-infrared ‘photosphere’ are similar for all three objects. Thus a low gravity ($\log g = 3.5$) object with $T_{\text{eff}} = 1000$ K ends up with cloud opacity that is very similar to a high gravity ($\log g = 5.5$) object with $T_{\text{eff}} = 1200$ K and consequently similar spectra and colors. Indeed Barman et al. (2011a) has already noted the similarity of SDSS 1516+30 to HR 8799b. This congruence between lower gravity and higher gravity models led to the initial surprise that the apparently cool planets seem to have clouds reminiscent of higher gravity—and warmer—L dwarfs.

The relative contribution of clouds to the opacity in individual photometric bands is depicted in Figure 9. This figure presents contribution functions for the J, H, K, L' , and M' bands for six different combinations of gravity, effective temperature, and cloud treatment. The contribution functions illustrate the fractional contribution to the emergent flux as a function of pressure in the atmosphere. In a cloud-free, $T_{\text{eff}} = 1000$ K, $\log g = 5.0$ atmosphere (left panel, Figure 9a) the L' flux emerges predominantly near $P = 0.6$ bar while the J -band flux emerges from near 8 bar. The contribution functions do not account for the effect of

cloud opacity, but rather show for each case where the flux would emerge from for that particular model if there were no clouds.

The middle two panels of Figure 9a and b illustrate the vertical location of the cloud layers for both $f_{\text{sed}} = 1$ and 2. The $f_{\text{sed}} = 2$ clouds are thinner and the cloud base is deeper since these less cloudy atmospheres are cooler than the $f_{\text{sed}} = 1$ case, as seen in the right hand panels. If the cloud deck lies above or overlaps the plotted contribution function of a given band then the emergent flux in that band will be strongly affected by the presence of the cloud. The figure makes clear that regardless of gravity thicker clouds impact more of the emergent spectra than thinner clouds. Clouds described by $f_{\text{sed}} = 2$ strongly impact J, H, and K bands, but are less important at L' , and M' . We conclude that at least for the effective temperature range inhabited by HR 8799 b, c, and d that clouds are most strongly impacting the observed spectra at wavelengths shorter than about $2.5 \mu\text{m}$ while the longer wavelength flux is primarily emerging from above the cloud tops. Figures such as this illustrate the value multi-band photometry has in both constraining not only the total emergent flux, but also the vertical structure of the clouds.

5.4. Evolution with a gravity-dependent L to T transition

The growing evidence that the cloudy to cloudless transition in field brown dwarfs depends on gravity (§2.1) is complemented by the published analyzes of the HR 8799 planets (including the present work) which all indicate that their atmospheres are cloudy and that they have T_{eff} well below the estimated $\sim 1400 \text{ K}$ limit of the L dwarf sequence. Thus, it appears that the atmospheres of lower gravity dwarfs and of imaged exoplanets retain their clouds to lower T_{eff} , which is supported by simple cloud model arguments (§2.2). As we have argued, this is the simplest interpretation of the fact that the HR 8799 planets have T_{eff} typical of cloudless T dwarfs but have evidently cloudy atmospheres. How is the evolution of brown dwarfs across the transition from cloudy to clear atmosphere affected?

The atmosphere of a brown dwarf largely controls its evolution because it acts as a surface boundary condition for the interior. A more opaque atmosphere (more clouds, or higher metallicity, for instance) slows the escape of radiation and increases the cooling time of the interior. In Saumon & Marley (2008), we looked at the evolution of brown dwarfs across the transition by assuming that the atmosphere was cloudy ($f_{\text{sed}} = 2$) down to $T_{\text{eff}} = 1400 \text{ K}$, and clear below 1200 K , with an linear interpolation of the atmospheric boundary condition in the transition regime. Qualitatively, this corresponds to increasing the sedimentation efficiency across the transition, one of the proposed explanations for the cloud clearing (§2.1). By converting the evolution sequences to magnitudes using synthetic spectra ($f_{\text{sed}} = 1$ for

cloudy atmospheres, and $f_{\text{sed}} = 4$ for “clear” atmospheres¹) a good match to the near-infrared color magnitude diagrams of field dwarfs was found from the cloudless late M dwarfs, along the cloudy L dwarf sequence, across the L/T transition and down to late T dwarfs.

We now extend this toy model to include a gravity-dependent range of T_{eff} for the transition to explore the consequences, at the semi-quantitative level, on the cooling tracks of brown dwarfs and exoplanets. In view of the success obtained for field dwarfs (of relatively high gravity) with the Saumon & Marley (2008) toy model, and the requirement that the lower gravity HR 8799 planets be cloudy at $T_{\text{eff}} \sim 1000$ K, we define the transition region to be $T_{\text{eff}} = 1400$ to 1200 K at $\log g = 5.3$ (cgs) and 900 to 800 K at $\log g = 4$ with a linear interpolation in between (Fig. 10). The cloudy boundary condition above the transition is based on our $f_{\text{sed}} = 2$ atmosphere models, and our cloudless models below the transition, as in Saumon & Marley (2008). Synthetic magnitudes are generated from the cooling tracks using our new $f_{\text{sed}} = 1$ and cloudless atmosphere models (Saumon et al. 2012).

The resulting cooling tracks of two low-mass objects of 5 and 20 M_J are shown in Fig. 11 where the same calculation, but based on a fixed T_{eff} transition (Fig. 10) is also displayed for comparison. It is immediately apparent that these low-mass objects, which retain their clouds to lower T_{eff} (~ 850 K for 5 M_J and ~ 1050 K for 20 M_J) with the prescribed gravity-dependent transition evolve along the L dwarf sequence longer and reach the region of the CMD occupied by the HR 8799 planets before they turn to blue $J - K$ colors as the cloud clears. Also remarkable is that in the transition region where the $J - K$ color changes from ~ 2 to ~ 0 , the low mass object is *fainter* in K than the higher mass object, the reverse of the situation for a transition that is independent of T_{eff} . This effect persists up to a cross over mass of $\sim 60 M_J$ above which the trend reverses (Fig. 10). This implies that low mass objects that are in the transition region should appear below (i.e. be dimmer) the field T0–T4 dwarfs, perhaps by up to 1–2 magnitudes. We note that the pile up of objects in the transition region reported in Saumon & Marley (2008) still occurs in this new calculation but it is more spread out in T_{eff} , as would be expected from the broader range of the transition in T_{eff} (Fig. 10).

We emphasize that this evolution calculation is a toy model that has been loosely adjusted to account for limited observational constraints. It reveals trends but is not quantitatively reliable. In particular, we have had to use $f_{\text{sed}} = 1$ to match the near infrared colors of the HR 8799 planets while our best fits give $f_{\text{sed}} = 2$ for all three planets. This reflects the fact that the models give different best-fit parameters when applied to a subset of the

¹These is not fully consistent with the values used for the evolution, but the effect on the evolution of this small difference in f_{sed} is small.

data, a well-known difficulty with current models (Cushing et al. 2008; Patience et al. 2012).

5.5. Mixing

Given the discussion in Section 1.3 regarding the prevalence of atmospheric mixing resulting in departures from chemical equilibrium in solar system giants and brown dwarfs, it is not surprising that mixing is also important in warm exoplanet atmospheres as well. Barman et al. (2011a) discuss the influence of non-equilibrium chemistry at low gravity and find that the CO/CH₄ ratio can become much larger than 1 in the regimes inhabited by the HR 8799 planets. Indeed we find that all of the best fitting models for each planet include non-equilibrium chemistry.

5.6. Future

Our experience in fitting the spectra of planet b in particular points to the importance of spectra in the analysis. Adding the H and K band spectra to the analysis results in much lower preferred masses than fitting photometric data alone. Thus we expect that additional spectral data will further inform future model fits. *kind of lame*

As noted in Section 2.1 one hypothesis for the nature of the L to T transition is that it involves partial clearing of the assumed global cloud cover. It is possible that models which include partial cloudiness may better describe the observed flux and Currie et al. (2011) have explored this possibility. Given the limited data available today we feel the addition of another free model parameter is premature and in any event we have found that brown dwarfs with partial cloud cover have an overall near-infrared spectrum that resembles a homogeneous dwarf with a thinner, homogenous global cloud (Marley et al. 2010).

Another method for characterizing these planets and probing atmospheric condensate opacity in self-luminous planets is by polarization (Marley & Sengupta 2011; de Kok et al. 2011). Marley & Sengupta (2011) found that rapidly rotating, homogeneously cloud-covered planets may show polarization fractions of around 1% if they are relatively low mass. de Kok et al. (2011) found that even when partial cloudiness is considered much larger polarization fractions are unlikely. However if this level of polarization could be measured in one of the HR 8799 planets this would confirm the presence of clouds and also place an upper limit on the planetary mass. Objects in this effective temperature range (near 1000 K) and with $\log g > 4$ are predicted to exhibit polarization well below 0.2%. Both SPHERE and GPI have polarization imaging modes, but it is not clear if they would have sufficient sensitivity

to place useful upper limits on the HR 8799 system.

6. Conclusions

We have explored the physical properties of three of the planets orbiting HR 8799 by fitting our standard model spectra to the available photometry and spectroscopy. Unlike most previous studies we have specified that models with a given $\log g$ and T_{eff} have a corresponding radius that is calculated from a self-consistent set of evolution models. Thus the radius of the planets is not a free parameter in our approach and indeed we find solutions with radii equal to those expected from evolution calculations. Unusually small radii are not required. We do include two other free parameters, the cloud sedimentation efficiency f_{sed} and the minimum atmospheric eddy mixing coefficient K_{zz} .

In agreement with all previous studies we find that the atmospheres of all three planets are cloudy, which runs counter to the expectation of conventional wisdom. However as we argue in Sections 2.1 and 2.2, finding clouds to be present at lower effective temperatures in lower gravity objects is fully consistent with trends already recognized among field L and T dwarfs and from basic atmospheric theory. We uniformly find that the best fitting value of the sedimentation efficiency f_{sed} is, in all cases, 2, which is typical of the value seen in pre-L/T transition field L dwarfs (Fig. 1) (Cushing et al. 2008; Stephens et al. 2009). We thus do not find the clouds in these objects to be “radically enhanced” (Currie et al. 2011) or to represent a “new class” (Madhusudhan et al. 2011) of atmospheres.

As have some previous authors (refs) we find that eddy mixing in nominally stable atmospheric layers is an important process for altering the chemical composition of all three planets. While we have not carried out a comprehensive survey of non-equilibrium models, we find that values of the eddy mixing coefficient near $\log K_{zz} \sim 4$ generally adequately reproduce the data. Such values are typical of those found for field L and T dwarfs (e.g., Stephens et al. 2009) and solar system giant planets (refs).

The best fitting values for the primary model parameters $\log g$ and T_{eff} are somewhat less secure. For HR 8799 b the H and K band spectra of Barman et al. (2011a) drive our fits to low masses of $\sim 3 M_J$. The photometry alone favors much higher masses, $\sim 25 M_J$ that are apparently ruled out by dynamical considerations. Fits for the remaining two planets in the system likewise generally favor higher masses, although there are some solutions that are consistent with masses near or below $\sim 10 M_J$ with ages consistent with the available constraints. For all three planets the photometry predicted by the best fitting model is generally consistent with the observed data with 1 to 2 standard deviations with the most

discrepant point generally being L' . We stress that all of these fits have radii that are appropriate for the stated effective temperature and gravity.

In conclusion the modeling approach that has successfully reproduced the spectra of field L and T dwarfs seems to also be fully applicable to the directly imaged planets. Nevertheless a larger range of model parameters, including metallicity, should be explored in order to fully characterize these objects as well as the planets yet to be discovered by the upcoming GPI, SPHERE, and other coronagraphs.

7. Acknowledgements

NASA provided support for this work via the Planetary Atmospheres Program (MSM), the Spitzer Space telescope Theoretical Research Program (DS). We thank Travis Barman and Bruce Macintosh for helpful conversations.

REFERENCES

- Ackerman, A. & Marley, M. S. 2001, *ApJ*, 556, 872.
- Allard, F., Hauschildt, P. H., Alexander, D. R., Tamanai, A., & Schweitzer, A. 2001, *ApJ*, 556, 357
- Artigau, É., Bouchard, S., Doyon, R., & Lafrenière, D. 2009, *ApJ*, 701, 1534
- Baines, K. H., et al. 2005, *Earth Moon and Planets*, 96, 119
- Baines, K. H., et al. 2005, *Earth Moon and Planets*, 96, 119
- Banfield, D., Gierasch, P. J., Bell, M., Ustinov, E., Ingersoll, A. P., Vasavada, A. R., West, R. A., & Belton, M. J. S. 1998, *Icarus*, 135, 230
- Barman, T. S., Macintosh, B., Konopacky, Q. M., & Marois, C. 2011, *ApJ*, 733, 65
- Barman, T. S., Macintosh, B., Konopacky, Q. M., & Marois, C. 2011, *ApJ*, 735, L39
- Becklin, E. E., & Zuckerman, B. 1988, *Nature*, 336, 656
- Blake, C. H., Charbonneau, D., White, R. J., Marley, M. S., & Saumon, D. 2007, *ApJ*, 666, 1198
- Bowler, B. P., Liu, M. C., Dupuy, T. J., & Cushing, M. C. 2010, *ApJ*, 723, 850
- Burgasser, A. J., Marley, M. S., Ackerman, A. S., Saumon, D., Lodders, K., Dahn, C. C., Harris, H. C., & Kirkpatrick, J. D. 2002, *ApJ*, 571, L151
- Burgasser, A. J.,Looper, D. L., Kirkpatrick, J. D., Cruz, K. L., & Swift, B. J. 2008, *ApJ*, 674, 451
- Burgasser, A. J., et al., 2010, *ApJ*, submitted
- Burgess, A. S. M., Moraux, E., Bouvier, J., et al. 2009, *A&A*, 508, 823
- Burningham, B., Pinfield, D. J., Leggett, S. K., et al. 2008, *MNRAS*, 391, 320
- Burrows, A., et al. 1997, *ApJ*, 491, 856
- Burrows, A., Sudarsky, D., & Hubeny, I. 2006, *ApJ*, 640, 1063
- Burrows, A., Sudarsky, D., & Hubeny, I. 2006, *ApJ*, 640, 1063

- Casewell, S. L., Dobbie, P. D., Hodgkin, S. T., Moraux, E., Jameson, R. F., Hambly, N. C., Irwin, J., & Lodieu, N. 2007, MNRAS, 378, 1131
- Casewell, S. L., Jameson, R. F., Burleigh, M. R., et al. 2011, MNRAS, 412, 2071
- Chauvin, G., Lagrange, A.-M., Dumas, C., Zuckerman, B., Mouillet, D., Song, I., Beuzit, J.-L., & Lowrance, P. 2004, A&A, 425, L29
- Cruz, K. L., Reid, I. N., Liebert, J., Kirkpatrick, J. D., & Lowrance, P. J. 2003, AJ, 126, 2421
- Cushing, M. C. et al. 2008, ApJ, 678,1372.
- Currie, T., et al. 2011, ApJ, 729, 128
- Dahn, C. C., et al. 2002, AJ, 124, 1170
- de Kok, R. J., Stam, D. M., & Karalidi, T. 2011, ApJ, 741, 59
- Fabrycky, D. C., & Murray-Clay, R. A. 2010, ApJ, 710, 1408
- Fegley, B. & Lodders, K. 1994, Icarus110, 117
- Fegley, B. & Lodders, K. 1996 ApJ, 472 L37
- Folkes, S. L., Pinfield, D. J., Kendall, T. R., & Jones, H. R. A. 2007, MNRAS, 378, 901
- Freedman, R., Marley, M., & Lodders, K. 2008, ApJS, 174, 504
- Freytag, B., Allard, F., Ludwig, H.-G., Homeier, D., & Steffen, M. 2010, A&A, 513, A19
- Frommhold, L., Abel, M., Wang, F., Li, X., & Hunt, K. L. C. 2010, American Institute of Physics Conference Series, 1290, 219
- Galicher, R., Marois, C., Macintosh, B., Barman, T., & Konopacky, Q. 2011, ApJ, 739, L41
- Geballe, T. R., Saumon, D., Leggett, S. K., et al. 2001, ApJ, 556, 373
- Geballe, T. R., Saumon, D., Golimowski, D. A., et al. 2009, ApJ, 695, 844
- Gelino, C. R. et al. 2002, ApJ, 577,433
- Gizis, J. E. 2002, ApJ, 575, 484
- Goldblatt, C. & Zahnle, K. 2010, Clim. Past Discuss. 6, 1163.

- Golimowski, D. A., et al. 2004, *AJ*, 127, 3516
- Goździewski, K., & Migaszewski, C. 2009, *MNRAS*, 397, L16
- Hauschildt, P. H., Allard, F., & Baron, E. 1999, *ApJ*, 512, 377
- Hubeny, I., & Burrows, A. 2007, *ApJ*, 669, 1248
- Hughes, A. M. et al. 2011, arxiv:1107.3153v1
- Isobe, T., Feigelson, E. D., & Nelson, P. I. 1986, *ApJ*, 306, 490
- Kirkpatrick, J. D. 2005, *ARAA*, 43, 195.
- Knapp, G. R., et al. 2004, *AJ*, 127, 3553
- Koen, C. 2003, *MNRAS*, 346, 473.
- Leggett, et al. 2002, *ApJ*, 564, 452
- Leggett, S. K., Marley, M. S., Freedman, R., Saumon, D., Liu, M. C., Geballe, T. R., Golimowski, D. A., & Stephens, D. C. 2007a, *ApJ*, 667, 537
- Leggett, S. K., Saumon, D., Marley, M. S., Geballe, T. R., Golimowski, D. A., Stephens, D., & Fan, X. 2007b, *ApJ*, 655, 1079
- Leggett, S. K., Saumon, D., Albert, L., et al. 2008, *ApJ*, 682, 1256
- Leggett, S. K., Cushing, M. C., Saumon, D., et al. 2009, *ApJ*, 695, 1517
- Leggett, S. K., Saumon, D., Burningham, B., et al. 2010, *ApJ*, 720, 252
- Liu, M. C., Leggett, S. K., Golimowski, D. A., Chiu, K., Fan, X., Geballe, T. R., Schneider, D. P., & Brinkmann, J. 2006, *ApJ*, 647, 1393
- Lodders, K. 1999, *ApJ*, 519, 793
- Lodders, K. 2003, *ApJ*, 591, 1220
- Lodders, K. & Fegley, B. 2002, *Icarus*, 155, 393
- Lodders, K. & Fegley, B. 2006, in *Astrophysics Update 2*, ed. J. W. Mason (Berlin: Springer), 1
- Looper, D. L., Gelino, C. R., Burgasser, A. J., & Kirkpatrick, J. D. 2008, *ApJ*, 685, 1183

- Luhman, K. L., et al. 2007, *ApJ*, 654, 570
- Madhusudhan, N., Burrows, A., & Currie, T. 2011, *ApJ*, submitted.
- Mainzer, A. K., et al. 2007, *ApJ*, 662, 1245
- Mainzer, A., Cushing, M. C., Skrutskie, M., et al. 2011, *ApJ*, 726, 30
- Marley, M. S., Saumon, D., Guillot, T., Freedman, R. S., Hubbard, W. B., Burrows, A., & Lunine, J. I. 1996, *Science*, 272, 1919
- Marley, M. S. 1998, *Brown Dwarfs and Extrasolar Planets*, 134, 383
- Marley, M. S., & McKay, C. P. 1999, *Icarus*, 138, 268
- Marley, M. S. et al. 2002, *ApJ*, 568, 335.
- Marley, M. S., Fortney, J., Seager, S., & Barman, T. 2007, *Protostars and Planets V*, 733
- Marley, M. S., Saumon, D., & Goldblatt, C. 2010, *ApJ*, 723, L117
- Marley, M. S., & Sengupta, S. 2011, *MNRAS*, 417, 2874
- Marois, C., Macintosh, B., Barman, T., Zuckerman, B., Song, I., Patience, J., Lafrenière, D., & Doyon, R. 2008, *Science*, 322, 1348
- Marois, C., Zuckerman, B., Konopacky, Q. M., Macintosh, B., & Barman, T. 2010, *Nature*, 468, 1080
- McKay, C. P., Pollack, J. B., & Courtin, R. 1989, *Icarus*, 80, 23
- Menard, F. & Delfosse, X. 2004, *Semaine de l’Astrophysique Francaise*, ed. F. Combes et al. (EDP-Sciences : Paris 2004) 305.
- Metchev, S. A., & Hillenbrand, L. A. 2006, *ApJ*, 651, 1166
- Miller, N., & Fortney, J. J. 2011, *ApJ*, 736, L29
- Moya, A., Amado, P. J., Barrado, D., et al. 2010, *MNRAS*, 406, 566
- Nakajima, T., Oppenheimer, B. R., Kulkarni, S. R., Golimowski, D. A., Matthews, K., & Durrance, S. T. 1995, *Nature*, 378, 463
- Noll, K. S., Geballe, T. R., & Marley, M. S. 1997, *ApJ*, 489, L87

- Oppenheimer, B. R., Kulkarni, S. R., Matthews, K., & van Kerkwijk, M. H. 1998, *ApJ*, 502, 932
- Orton, G., et al. 1996, *Science*, 272, 839
- Pierrehumbert, R.T. 1995, *J. Atmos. Sci.*, 52, 1784.
- Radigan, J., et al. 2011, *ApJ*submitted
- Roellig, T. L., et al. 2004, *ApJS*, 154, 418
- Saumon, D., Geballe, T. R., Leggett, S. K., et al. 2000, *ApJ*, 541, 374
- Saumon, D., Marley, M. S., Cushing, M. C., Leggett, S. K., Roellig, T. L., Lodders, K., & Freedman, R. S. 2006, *ApJ*, 647, 552
- Saumon, D., et al. 2007, *ApJ*, 656, 1136
- Saumon, D. & Marley, M. S. 2008, *ApJ*, 689, 1327.
- Sengupta, S. & Marley, M. S. 2011, submitted.
- Soummer, R., et al. 2011, *ApJ*, in press.
- Stephens, D. C. et al. 2009, *ApJ*, 702,154.
- Stumpf, M. B., Brandner, W., Bouy, H., Henning, T., & Hippler, S. 2010, *A&A*, 516, A37
- Su, K. Y. L., Rieke, G. H., Stapelfeldt, K. R., et al. 2009, *ApJ*, 705, 314
- Sudol, J. J. & Haghighipour, N. 2012, arXiv:1201.0561v2
- Tinney, C. G., Burgasser, A. J., Kirkpatrick, J. D., & McElwain, M. W. 2005, *AJ*, 130, 2326
- Tokunaga, A. T., Kobayashi, N., Bell, J., et al. 1998, *Proc. SPIE*, 3354, 512
- Tokunaga, A. T., Simons, D. A., & Vacca, W. D. 2002, *PASP*, 114, 180
- Toon, O., McKay, C., & Ackerman, T. 1989, *J. Geophys. Res.*, 94, D13 16287-16301
- Tsuji, T., & Nakajima, T. 2003, *ApJ*, 585, L151
- Tsuji, T., Nakajima, T., & Yanagisawa, K. 2004, *ApJ*, 607, 511
- van Leeuwen, F. 2007, *A&A*, 474, 653
- Vrba, F. J., et al. 2004, *AJ*, 127, 2948

- Westphal, J. A. 1969, *ApJ*, 157, L63
- Westphal, J. A., Matthews, K., & Terrile, R. J. 1974, *ApJ*, 188, L111
- Yurchenko, S. N., Barber, R. J., & Tennyson, J. 2011, *MNRAS*, 413, 1828
- Zuckerman, B., Rhee, J. H., Song, I., & Bessell, M. S. 2011, *ApJ*, 732, 61
- Burgasser, A.J., Kirkpatrick, J.D., Cruz, K. L., Reid, N. I., Leggett, S. K., Liebert, J., Burrows, A. & Brown, M. 2006, *ApJS*, 166, 585
- Dahn, C. C., Harris, H. C., Vrba, F. J., Guetter, H. H., Canzian, B., Henden, A. A., Levine, S. E., Luginbuhl, C. B., Monet, A. K. B., Monet, D. G., and 8 coauthors, 2002, *AJ*, 124, 1170
- Liu, M.C. & Leggett, S.K. 2005, *ApJ*, 634, L616
- Marocco, F., Smart, R.L., Jones, H.R.A., Burningham, B., Lattanzi, M.G., Leggett, S.K., Lucas, P.W., Tinney, C.G., Adamson, A., Evans, D.W., and 4 coauthors, 2010, *A&A*, 524, 38
- McCaughrean, M.J., Close, L.M., Scholz, R.-D., Lenzen, R., Biller, B., Brandner, W., Hartung, M. & Lodieu, N. 2004, *A&A*, 413, 1029
- Patience, J., King, R. R., De Rosa, R. J., Vigan, A., Witte, S., Rice, E., Helling, Ch., & Hauschildt, P. H. 2012, *astro-ph ArXiv:1201.3921*
- Perryman, M. A. C., et al. 1997, *A&A*, 323, L49
- Saumon, D., Marley, M. S., Abel, M., Frommhold, L., & Freedman, R. S. 2012, submitted to *ApJ*
- Tinney, C. G., Burgasser, A. J. & Kirkpatrick, J. D. 2003, *AJ*, 126, 975
- Vrba, F. J., Henden, A. A., Luginbuhl, C. B., Guetter, H. H., Munn, J. A., Canzian, B., Burgasser, A. J., Kirkpatrick, J. D., Fan, X., Geballe, T. R., and 5 coauthors 2004, *AJ*, 127, 2948

Table 1. Summary of Derived Planet Properties

Planet	Reference ¹	Mass (M_{Jup})	$\log g$	T_{eff} (K)	$R(R_{\text{J}})$	age (Myr)
b ²	B11a	0.1 – 3.3	3.5 ± 0.5	1100 ± 100	0.63 - 0.92	30 – 300
	C11	5 – 15	4 – 4.5	800 – 1000	...	30 – 300
	G11	1.8	4	1100	0.69	...
	M11	2 – 12	3.5 – 4.3	750 – 850	...	10 – 150
	This work:					
	photometry alone					
	phot. & spectra		3.48	1000 ± 25		
c	C11	7 – 17.5	4 – 4.5	1000 – 1200	...	30 – 300
	G11	1.1	3.5	1200	0.97	...
	M11	7 – 13	4 – 4.3	950 – 1025	...	30 – 100
	This work			4.7 ± 0.3	1070 ± 100	
d	C11	5 – 17.5	3.75 – 4.5	1000 – 1200	...	30 – 300
	G11	6	4.0	1100	1.25	...
	M11	3 – 11	3.5 – 4.2	850 – 1000	...	10 – 70
	This work			4.5 ± 0.3	1060 ± 110	

¹B11a=Barman et al. (2011a); C11=Currie et al. (2011); G11 = Galicher et al. (2011); M11=Madhusudhan et al. (2011)

²Parameters derived by Bowler et al. (2010) are not listed because of very large scatter depending upon various assumptions.

Table 2. Photometric Data for HR 8799 Planets

Planet	Band	Abs. Mag.	Ref. ¹
b	z	18.24 ± 0.29	C11
	J	16.52 ± 0.14	C11
	H	14.87 ± 0.17	M08
	K _s	14.05 ± 0.08	M08
	[3.3]	13.96 ± 0.28	C11
	L'	12.68 ± 0.12	C11
	M'	13.07 ± 0.30	G11
c	z	> 16.48	C11
	J	14.65 ± 0.17	M08
	H	13.93 ± 0.17	M08
	K _s	13.13 ± 0.08	M08
	[3.3]	12.64 ± 0.20	C11
	L'	11.83 ± 0.07	C11
	M'	12.05 ± 0.14	G11
d	z	> 15.03	C11
	J	15.26 ± 0.43	M08
	H	13.86 ± 0.22	M08
	K _s	13.11 ± 0.12	M08
	[3.3]	> 11.63	C11
	M'	11.67 ± 0.35	G11

¹C11=Currie et al. (2011)

M08=Marois et al. (2008)

G11=Currie et al. (2011)

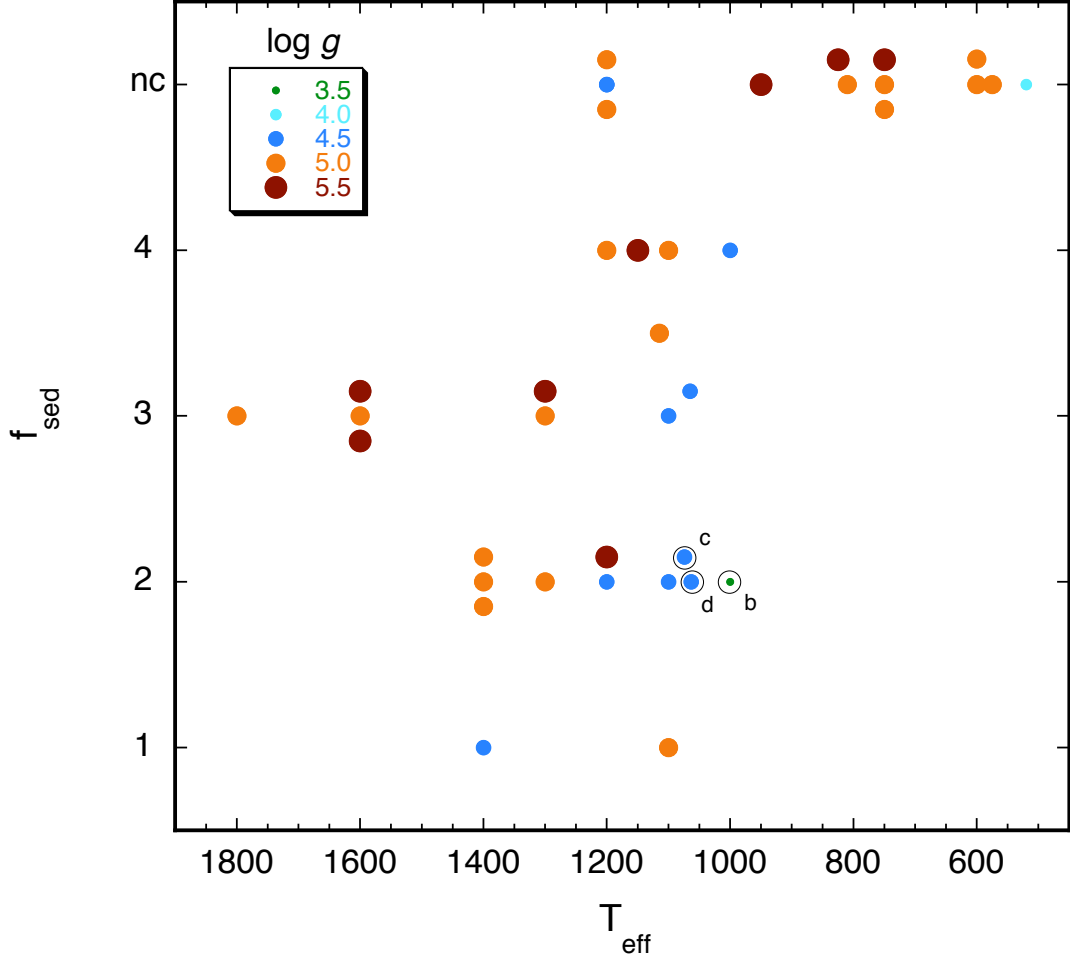


Fig. 1.— Model parameters f_{sed} and T_{eff} as derived by various applications of Marley & Saumon atmosphere and evolution models. Size of dot reflects derived $\log g$ (cm s^{-2}) and ‘nc’ denotes cloudless models (note that ‘nc’ is arbitrarily plotted at $f_{\text{sed}} = 5$). Points which would otherwise overlap are slightly offset vertically. The HR 8799 points from the analysis here are circled and labeled with planet designator. Remaining points are from Geballe et al. (2001); Mainzer et al. (2007); Leggett et al. (2007a, 2008); Geballe et al. (2009); Leggett et al. (2009); Stephens et al. (2009); Mainzer et al. (2011) although fits to unresolved binaries and objects with very poorly constrained properties (e.g., Gl 229 B with $\log g$ uncertain by a full dex) are excluded. Uncertainties in the remaining model fits are typically ± 100 K in effective temperature, ± 0.25 dex in $\log g$, and ± 0.5 in f_{sed} , although the uncertainty analysis is not uniform across the various sources.

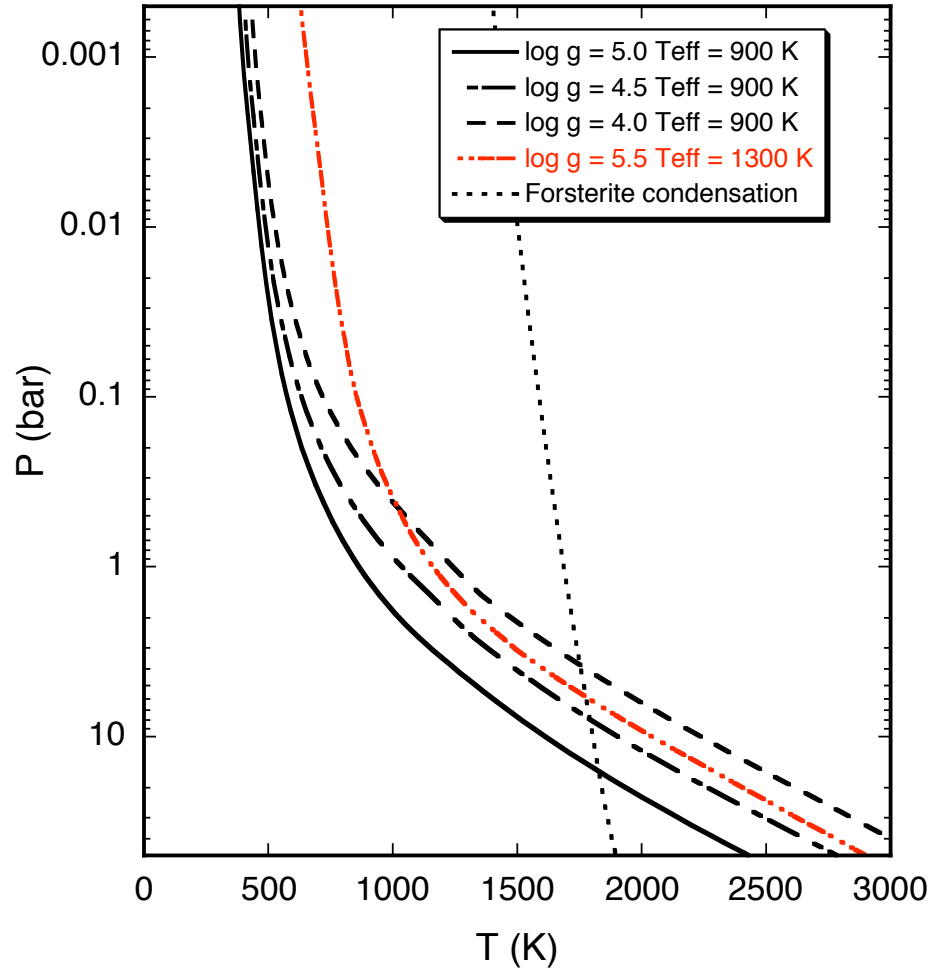


Fig. 2.— Model atmosphere temperature-pressure profiles for cloudy brown dwarfs and planets assuming $f_{\text{sed}} = 2$ (Ackerman & Marley 2001). Each profile is labeled with $\log g$ and T_{eff} of the model. The condensation curve for forsterite is shown with a dotted line.

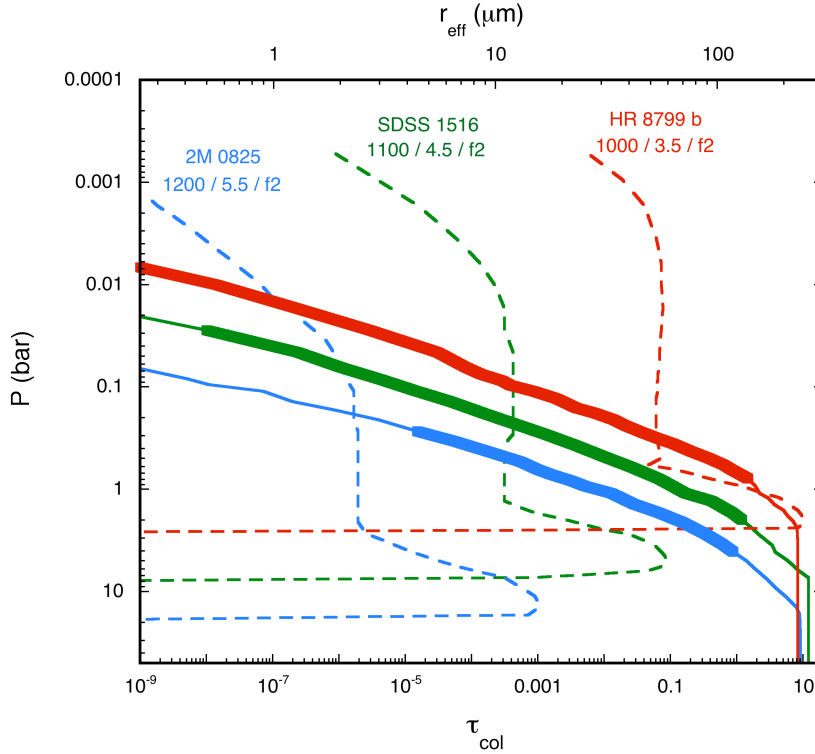


Fig. 3.— Silicate cloud properties as computed by the Ackerman & Marley (2001) cloud model for the best-fitting models for three objects, left to right, 2MASS 0825+21, SDSS 1516+30 and HR 8799b (this work for the latter and Stephens et al. (2009) for the others). Dashed curves show the effective radius, r_{eff} of the particles on the top axis and the column optical depth as measured from the top of the atmosphere assuming geometric optics on the bottom axis. Thicker lines denote the region of the cloud which lies within the $\lambda = 1$ to $6 \mu\text{m}$ photosphere. Other modeled clouds are not shown for clarity.

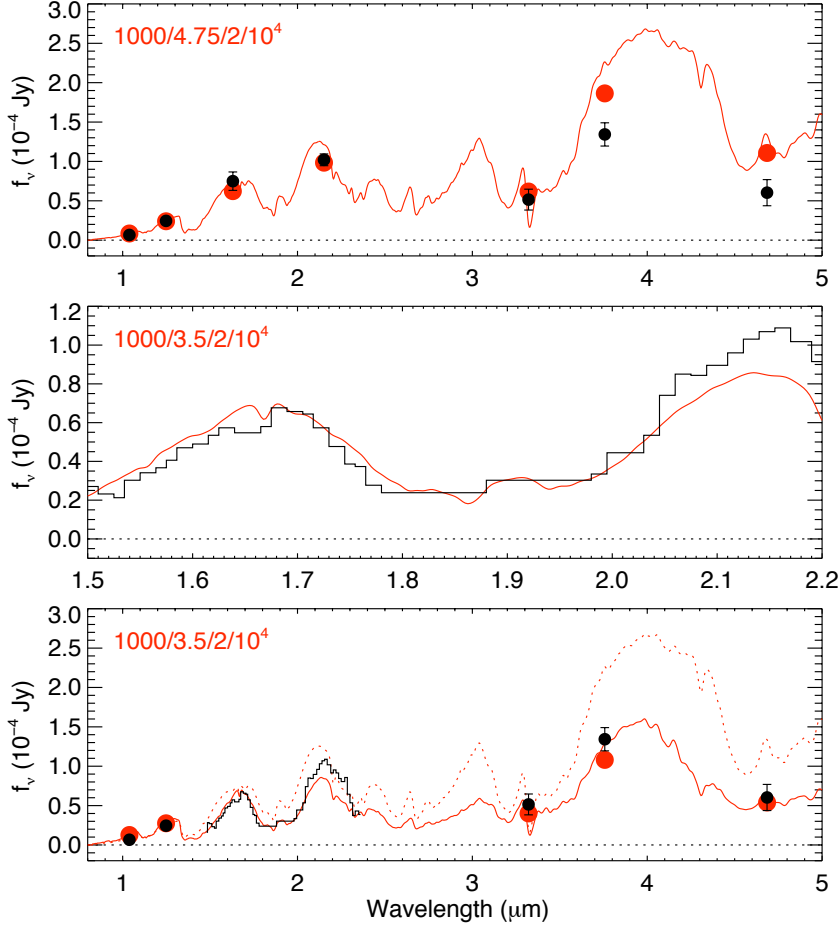


Fig. 4.— Observed (black) and model (red) photometry and spectra (see Table 1 and Barman et al. (2011a)) for HR 8799b. The top panel shows the model that best fits the photometry alone. The middle panel is the fit to only the observed spectrum and the lower panel shows the solution that best fits both the photometry (excluding H and K bands) and spectroscopy simultaneously (which turns out to be the same low-gravity model as in the middle panel). The high gravity solution is also shown in the lower panel as a dotted line. Models are identified in the upper left hand corner of each panel by $T_{\text{eff}}/\log g/f_{\text{sed}}/\log K_{zz}$. Model fluxes and photometry have been computed for radii specific to the T_{eff} and $\log g$ of the atmosphere model at a distance of 39.4 pc.

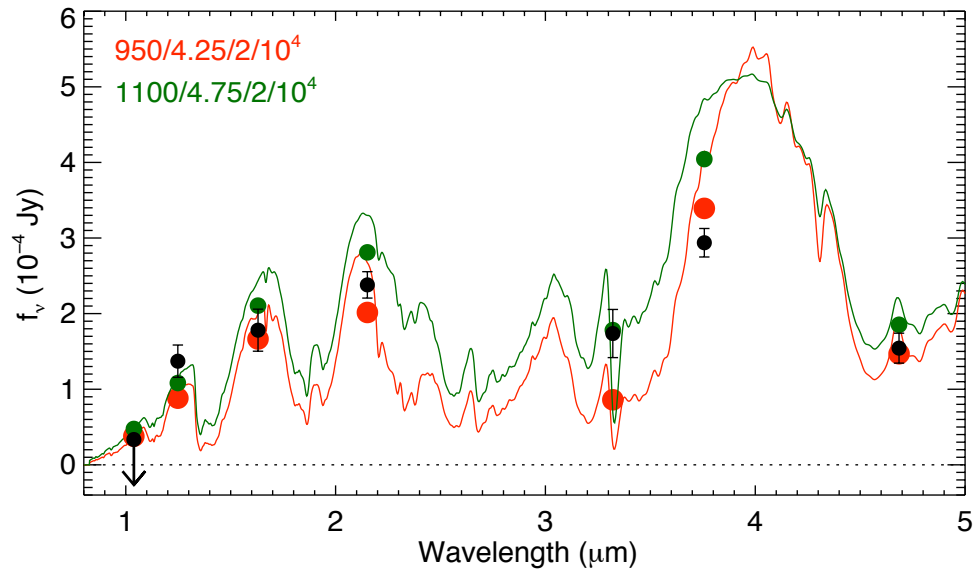


Fig. 5.— The two best fitting model spectra for HR 8799 c. Observed photometry (see Table 2) is shown in black, high and low gravity solutions in green and red, respectively. The two solutions correspond to the centers of the two best fitting ‘islands’ in the contour plot shown in Figure 5b. Models are labeled as in Figure 3.

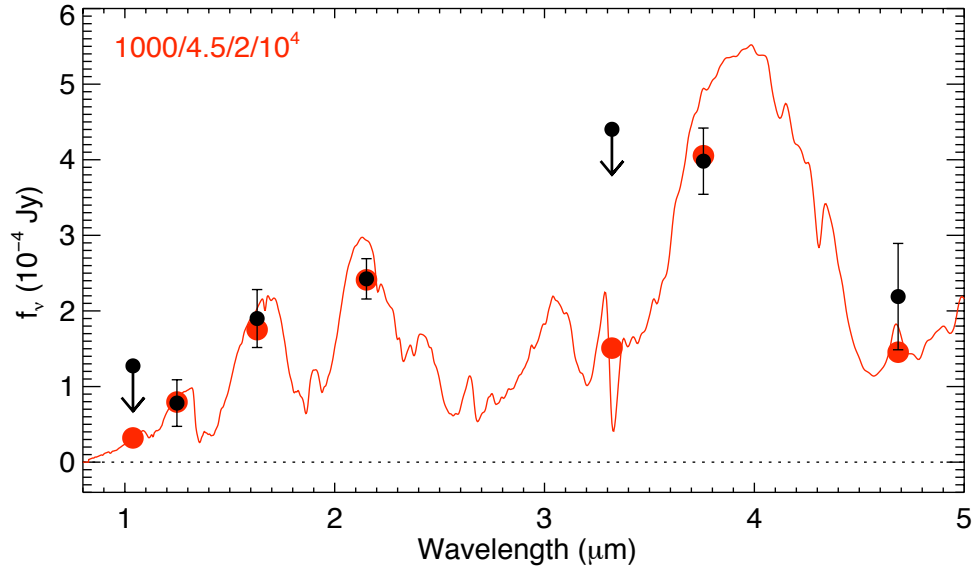


Fig. 6.— The best fitting model for HR 8799 d. Observed photometry (see Table 1) is shown in black; model photometry is indicated by the red dots. Model is labeled as in Figure 3.

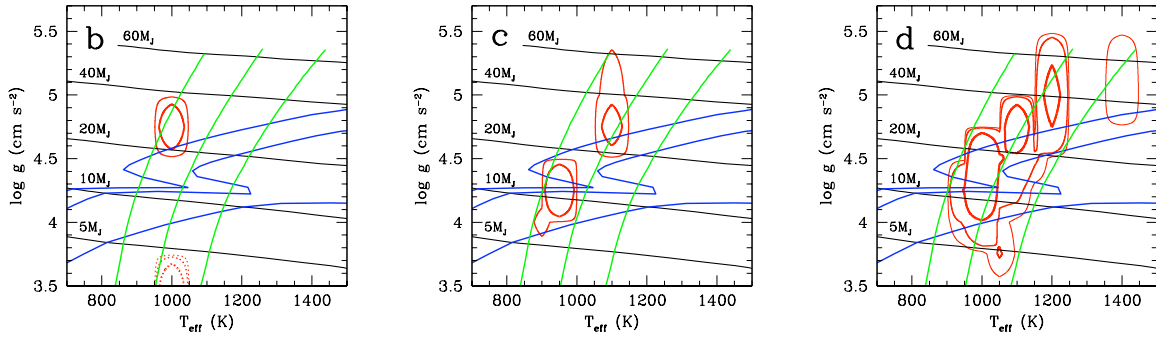


Fig. 7.— Contours illustrate domain of best-fitting models on the $\log g - T_{\text{eff}}$ plane. For each planet three contours are shown which encircle those model parameters that fit the observed data within 1, 2, and 3- σ (red, thick to thin contours). Evolution tracks from Saumon et al. (2007) are shown as labeled black curves; planets evolve from right to left with time across the diagram as they cool and contract. Blue curves are isochrones at (bottom to top) 30, 160, and 300 Myr; kinks in the older two isochrones arise from deuterium burning (objects burning D are substantially hotter than lower mass objects of the same age). Green curves are constant luminosity curves at (left to right) $\log L/L_{\odot} = -5, -4.75, -4.5$. For planet b solid contours denote fits to only the photometry while dashed curves are fits to photometry and H and K-band spectra.

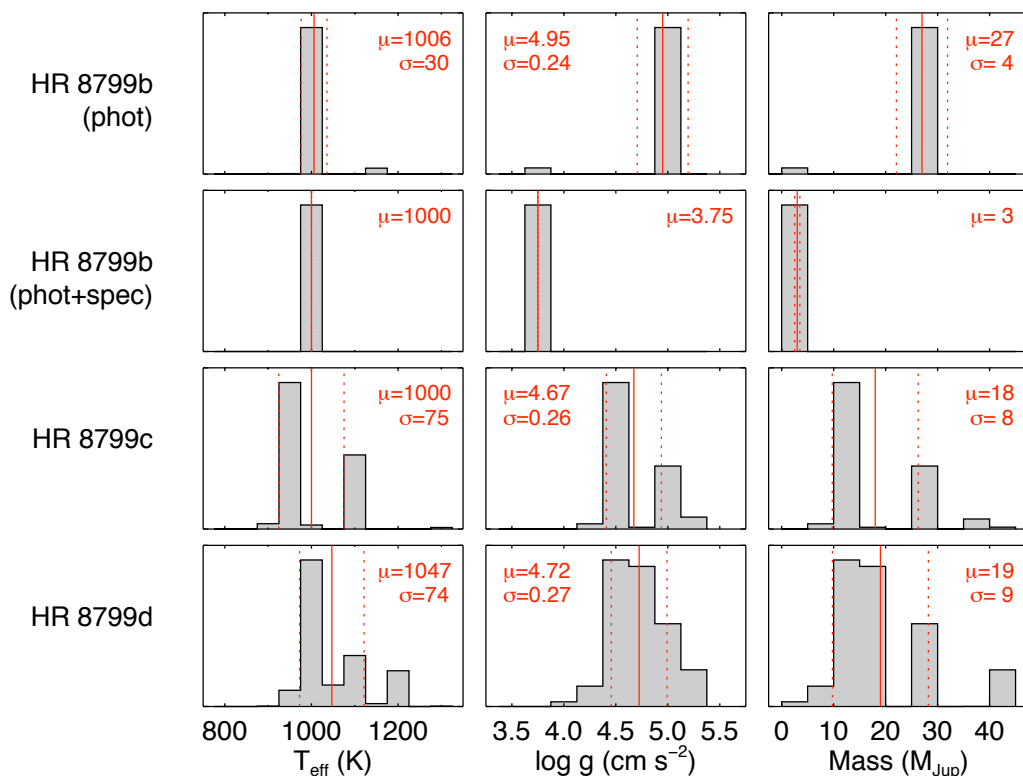


Fig. 8.— Histogram depicting the relative quality of fit of various model parameters to planets HR 8799 b, c, and d. For planet b two sets are shown, one for the fits only to the photometry (‘phot’) and one to both the photometry and spectroscopy (‘phot+spec’). The T_{eff} and $\log g$ histograms can be thought of as the projection of the contours shown in Figure 6 onto these two orthogonal axes. In each case the mean of the fit and the size of the standard deviation is indicated by μ and σ , respectively. These quantities are in turn illustrated by the solid and dashed vertical lines. The third column of histograms depicts the same information as the first two, but for the mass corresponding to each (T_{eff} , $\log g$) pair, as computed by the evolution model.

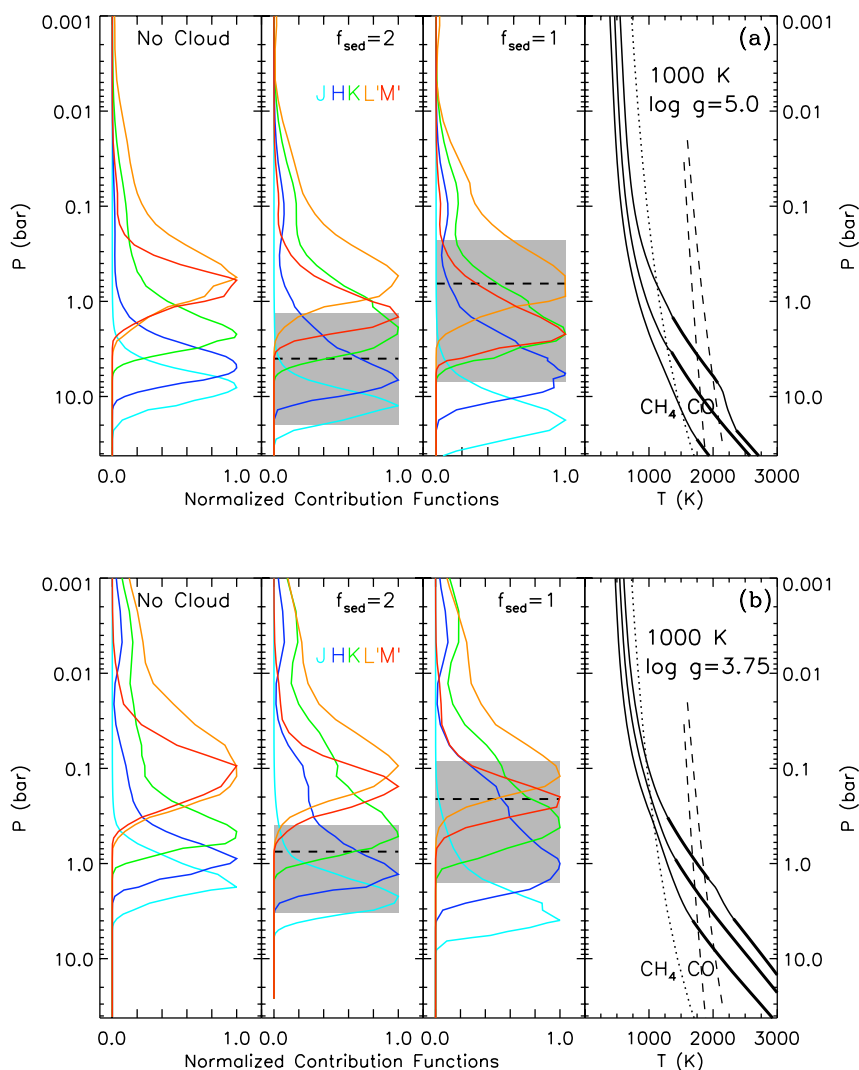


Fig. 9.— Illustration of the effect of gravity and cloud properties on modeled emergent flux for $T_{\text{eff}} = 1000$ K and $\log g = 5.0$ (a) and 3.75 (b). Both plots (a) and (b) consist of four sub-panels. The right-most sub-panel depicts the $T(P)$ profiles for three atmosphere models with the indicated T_{eff} and $\log g$. In each case the profiles are for (left to right) for cloudless, $f_{\text{sed}} = 2$, and 1 models. Diamonds denote the top of the convection zones. In cases with a second, detached zone the base of the upper zone is shown by a triangle. The dotted line denotes chemical equilibrium between CO and CH₄. The dashed lines are the condensation curves for Fe (right) and Mg₂SiO₄ (left). The cloud base is expected at the point where the condensation curves cross the $T(P)$ profiles. Remaining panels show the contribution function (see text) averaged over the J , H , K , L' and M' bandpasses (colored lines) for each of the three model cases. The shaded regions denote the extent of the cloud, extending from the point where the integrated optical depth from the top of the model is 0.1 to the cloud base. Thick horizontal dashed line denotes cloud $\tau = 2/3$.

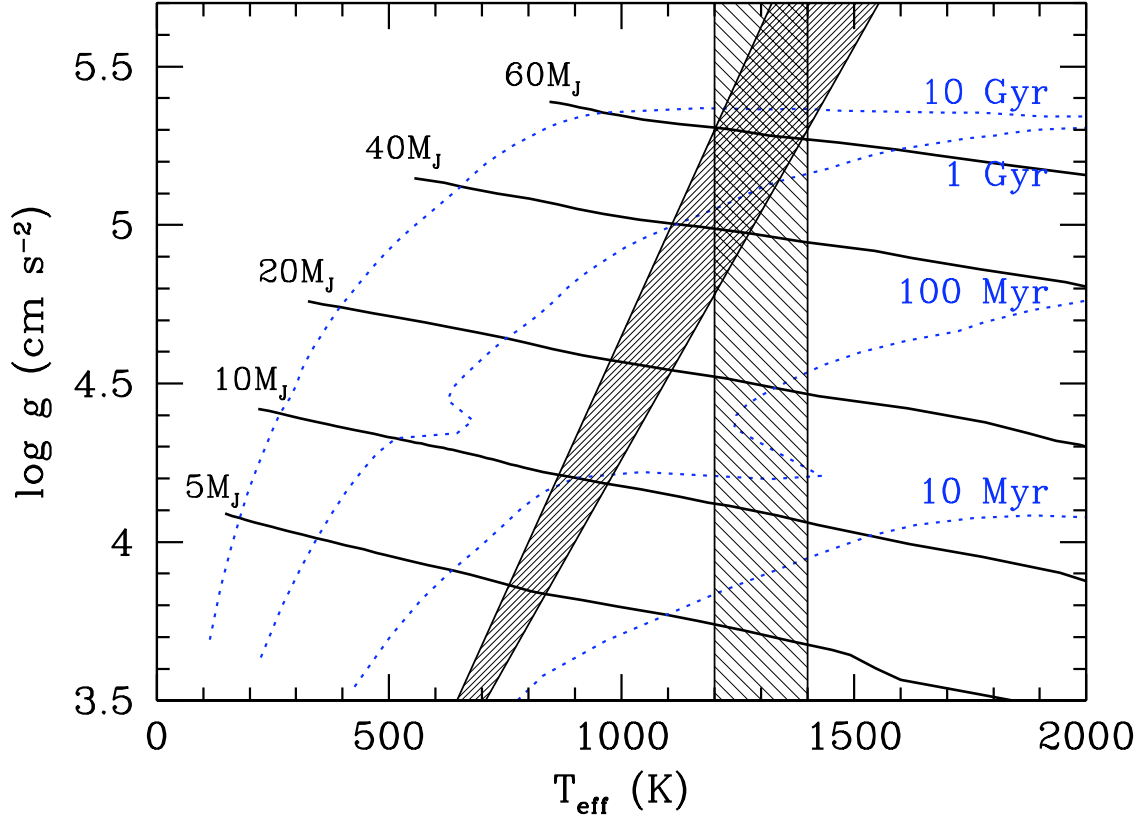


Fig. 10.— Definition of the transition from cloudy to cloudless surface boundary condition for the evolution. This represents a toy model of the L/T transition. In the hybrid toy model of Saumon & Marley (2008), the transition region was chosen to be independent of gravity and the cloud clearing occurred between $T_{\text{eff}} = 1400$ and 1200 K (lightly hashed area). To the right of the transition region shown, the surface boundary condition is based on cloudy atmosphere models; to the left, on cloudless atmospheres; and on a simple interpolation in the transition region. Here, we present an evolution calculation where the T_{eff} range of the transition is made gravity dependent (densely hashed area). Representative cooling tracks are shown in black and labeled by the mass. Isochrones are the blue dotted lines.

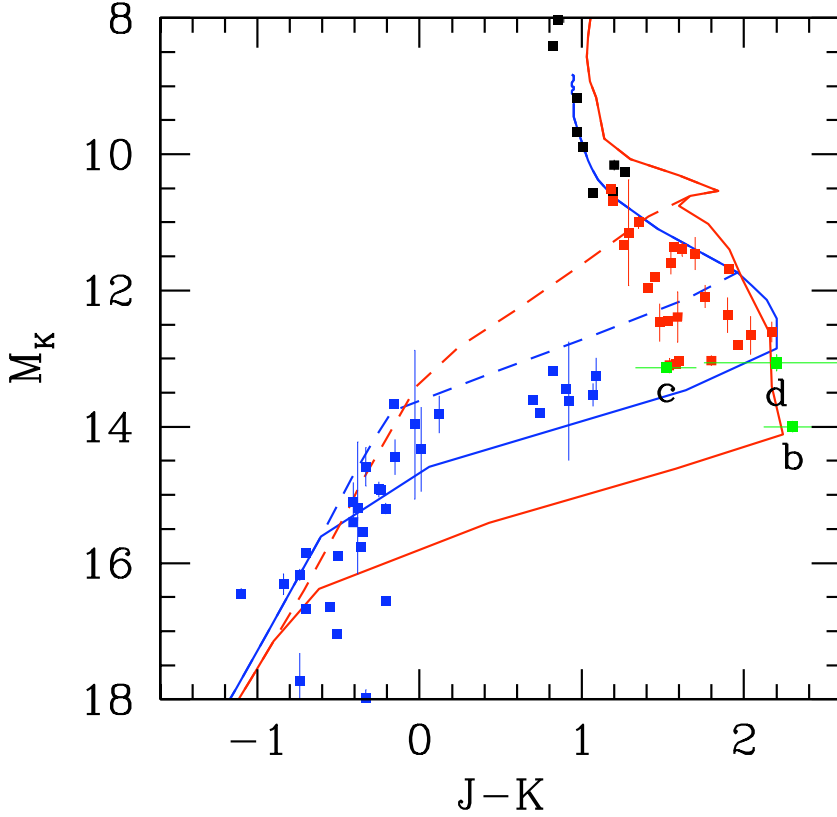


Fig. 11.— Examples of cooling tracks for brown dwarfs of $5 M_J$ (red) and $20 M_J$ (blue) in a M_K vs. $J - K$ (MKO system) color-magnitude diagram where the transition from cloudy ($f_{\text{sed}} = 1$) to cloudless atmospheres is taken into account explicitly as in Saumon & Marley (2008). Dashed lines show the evolution when the transition occurs over a fixed range of T_{eff} that is independent of gravity, solid lines show the evolution for the gravity-dependent transition (see Fig. 10). The planets in the HR 8799 planets are shown with green symbols while resolved field objects are shown in black (M dwarfs), red (L dwarfs) and blue (T dwarfs). The photometry is from Leggett et al. (2002), Knapp et al. (2004), Marocco et al. (2010) (McCaughrean et al. 2004), (Burgasser et al. 2006), and (Liu & Leggett 2005). The parallaxes are from Perryman et al. (1997), Dahn et al. (2002), Tinney et al. (2003), Vrba et al. (2004), Marocco et al. (2010), and various references in Leggett et al. (2002).